Auroral Acceleration at the Northern Magnetic Pole During Sub-Alfvénic Solar Wind Flow at Earth

J. E. Waters[1], L. Lamy[2,1], S. Milan[3], M. -T. Walach[4], E. Chané[5]

[1]Aix Marseille Univ, CNRS, CNES, LAM, Marseille, France
[2]Observatoire de Paris, LESIA, PSL Research University, CNRS, Sorbonne Universit ´e, University of Paris, Meudon, France
[3]School of Physics and Astronomy, University of Leicester, Leicester LE1 7RH, UK
[4]Physics Department, Lancaster University, Bailrigg, Lancaster, LA1 4YW, UK
[5]Lycée Athénée de Luxembourg, 24 boulevard Pierre Dupong, 1430, Luxembourg

Key Points:

- Unexpected auroral activity observed in radio and UV wavelengths during rare sub-Alfvénic configuration of the magnetosphere.
- UV aurora exhibit a polar spot in the northern hemisphere, colocated with electron precipitation and auroral kilometric radiation.
- High-latitude dayside aurora, with the specific morphology of a space hurricane, is suggested as the mechanism driving localised auroral activity.

Corresponding author: J. E. Waters, `james.waters@lam.fr`

Abstract

Between 23-25 May 2002 the solar wind, due to very low plasma density, became sub-Alfvénic for enough time to promote the establishment of Alfvén wings that can limit typical solar wind-magnetosphere coupling. During this interval, the interplanetary magnetic field (IMF) was oriented northward and duskward, with a slightly dominant B_Y component; driving of the magnetosphere was expected to be low. Many signatures are used to assess solar wind-magnetosphere-ionosphere coupling, including ultraviolet (UV) observations of the auroral zone to infer monoenergetic electron precipitation and radio observations of auroral kilometric radiation (AKR) to infer the development of the auroral acceleration region. Observing these signatures with the IMAGE (Imager for Magnetopause-to-Aurora Global Exploration) and Wind spacecraft, we find evidence of auroral acceleration that allowed amplification of AKR to similar intensities as during super-Alfvénic coupling. This coincides with polar electron aurora around 8° square in latitude and at magnetic latitudes greater than 88°. The multipoint radio observations imply sources are generated along a constrained flux tube. Given the primary coincidence of AKR and the electron polar spot ∼3 hours following the incidence of minimally sub-Alfvénic ($M_A \sim 0.4$) at Earth, this acceleration occurs while the Alfvén wings are most complete. Given the IMF conditions, auroral morphology of the polar spot and the inference of an upward field-aligned current, the magnetospheric dynamics are most related to those of the high-latitude dayside aurora (HiLDA). These observations are the first to show AKR amplification from HiLDA and during a sub-Alfvénic magnetosphere, highlighting the possibility of strong localised coupling under quiet geomagnetic conditions.

Plain Language Summary

When the solar wind becomes sub-Alfvénic, the level of interaction with the terrestrial magnetosphere can be suppressed due to its structure becoming highly perturbed. Sub-Alfvénic solar wind is a rare occurrence, however; one of the longest duration sub-Alfvénic events occurred between 23-25 May 2002 and allowed enough time for the magnetosphere to change configuration. With observations of the aurora in ultraviolet (UV) and radio wavelengths (in the high latitude ionosphere and along co-located magnetic field lines, respectively) we find evidence of particle acceleration into the polar atmosphere during this event. This acceleration is highly constrained, producing localised electron aurora often centred on the magnetic pole. The solar wind conditions and the magnetospheric observations suggest the observed dynamics are related to known phenomena that occur during super-Alfvénic conditions, observed here for the first time during this abnormally quiet magnetospheric state and with associated radio emissions. These observations highlight the possibility of localised interactions that can be as intense as typical cases, even when conditions imply a quiet magnetosphere.

1 Introduction

The dynamic coupling between the solar and terrestrial magnetic environments is largely dependent on the plasma conditions of the solar wind as it impacts Earth; namely the solar wind density, speed, and the magnitude and orientation of the interplanetary magnetic field (IMF) (e.g. Wilcox et al., 1967; Burton et al., 1975; Gosling et al., 1990; Vennerstroem, 2001; Kilpua et al., 2017; Marques de Souza Franco et al., 2021). The upstream solar wind and its plasma parameters are time-variable with changing conditions on the sun, and typical, super-Alfvénic conditions and their resulting effect on the terrestrial magnetosphere are well explored. The IMF B_Z component, for example, varies often, with dramatic changes in the level of magnetospheric disturbance; a southward ($B_Z < 0$) IMF component produces a higher level of geomagnetic disturbance than a northward ($B_Z > 0$) component (Kamide et al., 1977; Nakai & Kamide, 1983; Brautigam et al., 1991; Kullen & Karlsson, 2004; Zhang et al., 2004) due to a greater magnetic reconnection rate at the dayside, subsolar magnetopause (Sonnerup, 1974; Akasofu, 1981). With the former, a global circulation of plasma known as the Dungey cycle (Dungey, 1961, 1965) can occur throughout the magnetosphere. This results in the energisation of the ring current, the auroral electrojets and other global current systems. In general, the Dungey cycle allows solar wind plasma to enter and circulate throughout the magnetosphere, inciting geomagnetic storms, for example (Baker et al., 1981; Gonzalez et al., 1994; Coleman et al., 2001; Milan et al., 2007). Well-known auroral morphology is formed in the high latitude ionosphere (at magnetic latitudes between 65°-80° depending on the level of geomagnetic activity) due to the bulk precipitation of electrons and protons along magnetic field lines, which precedes ultraviolet (UV) and optical emission from excited neutral species in the ionosphere (Feldstein & Starkov, 1970; Strickland et al., 1983; Christensen et al., 1987). The brightest, discrete auroral forms are produced from so-called monoenergetic electron beams when fast plasma flows follow reconnection events in the magnetotail (Hones, 1979; Lin & Hoffman, 1982; Kepko et al., 2009). Such events occur during substorms, for example, where energetic plasma reaches the nightside ionosphere at high, auroral latitudes via Birkeland or field-aligned currents (FACs) (Zmuda et al., 1966; Iijima & Potemra, 1976, 1978; Kamide et al., 1981; Juusola et al., 2011). With this, ionospheric currents develop close to midnight magnetic local times (MLTs) that then travel westward, producing bright, discrete aurora at a wide range of dusk/nightside MLTs (Akasofu, 1964; McPherron et al., 1973; Rothwell et al., 1984; Elphic et al., 1998; Milan et al., 2009; Despirak et al., 2020).

Under northward IMF, the configuration of magnetic reconnection differs greatly. In this case, magnetic reconnection occurs at much higher magnetic latitudes in one or both hemispheres (Reiff & Burch, 1985; Gosling et al., 1991; Østgaard et al., 2005). The resulting plasma motion leads to distinct convection patterns that are more spatially constrained than the global circulation induced under southward IMF, and the magnetosphere is less disturbed (Menietti & Burch, 1987; Crooker, 1992; Milan et al., 2020). Various proton and electron auroral phenomena have been identified with northward IMF conditions (Hones et al., 1989; Zhu et al., 1997; Fear et al., 2015; Milan et al., 2022), such as proton aurora following direct precipitation into the cusp (Crooker, 1979; Sandholt et al., 1996) as well as more complex dynamics that generate high-latitude dayside aurora (HiLDA) (Frey et al., 2003; Carter et al., 2018). Both phenomena see precipitation into the ionosphere poleward of the main auroral oval but on the dayside, often with a dusk- or dawn-ward bias depending on the orientation of the IMF y-component (Cowley, 1981; Ridley et al., 1998; Grocott & Milan, 2014). In the case of HiLDA, the high latitude lobe reconnection and resulting convection patterns that drive these dynamics sees electrons and protons enter the magnetosphere from the solar wind, with electrons particularly contributing to the upward FACs at the centre of clockwise-rotating convection cells. Space hurricanes are a phenomena closely related to HiLDA, with similar driving conditions (Milan et al., 2000; Q. H. Zhang et al., 2021; Lu et al., 2022). An upward FAC is produced with its ionospheric footprint eventually established at the magnetic pole following continued lobe reconnection at high magnetic latitudes with a dominant IMF B_Y component. The aforementioned coupling dynamics usually occur under super-Alfvénic solar wind conditions.

Auroral kilometric radiation (AKR) is a non-thermal radio emission generated by the electron cyclotron maser instability (ECMI) along magnetic field lines in the auroral acceleration region, and is often observed during periods of intense coupling such as substorms and geomagnetic storms. It is typically observed at frequencies between 100-400 kHz, with a peak intensity around 200 kHz, but can also be observed between frequencies of ~50-800 kHz (Gurnett, 1974; Benson et al., 1980; Morioka et al., 2013). For a sufficient growth rate to produce emission, a plasma cavity that hosts a horseshoe electron distribution function, often seen with monoenergetic electron beams on the order of a few keV, is required (Ergun et al., 2000; Treumann, 2006). As such, AKR sources are often found colocated with bright, discrete aurora in the high latitude, auroral ionosphere, following energetic electron precipitation from active acceleration regions (Green et al., 1982; Huff et al., 1988; Menietti et al., 2011). The resonance condition of the ECMI is such that AKR is emitted close to the electron gyrofrequency, with lower frequency emission produced from higher altitude sources. After being produced in the source region, AKR is refracted along the edges of the cavity before escaping at highly oblique angles to the magnetic field. This creates an approximately conical illumination region close to the tangent plane of the host magnetic field line (Mutel et al., 2008). When observing many AKR sources, as is typically the case for a remote spacecraft, a broad region of space is illuminated. Since AKR sources are colocated with discrete aurora however, they are best observed from dusk-nightside MLTs (Alexander & Kaiser, 1976; Mutel et al., 2004; Fogg et al., 2022). AKR has also been found to correspond to other auroral components nearer the pole or on the dayside (Hanasz et al., 2003), such as cusp aurora (Alexander & Kaiser, 1977) and transpolar arcs (Pedersen et al., 1992). Statistical analyses of observations from the Wind spacecraft show differences of up to 3 orders of magnitude between average AKR intensities observed from the nightside and those observed from the dayside (Waters et al., 2022). For individual cases, the viewing position is therefore of primary importance to properly interpret the observations, and such limitations can be countered by using multipoint observations (Hashimoto et al., 1998; R. R. Anderson et al., 2005; Waters, Jackman, et al., 2021; Waters et al., 2023), as is the case here.

In rare cases, the solar wind density can become low enough for it to become sub-Alfvénic, as defined by the ratio of the solar wind speed with the Alfvén speed. The Alfvén Mach number (M_A) is given by equation 1, where v is the solar wind speed, ρ_p is the proton mass density in the solar wind, μ_0 is the permeability of free space, and B is the total magnitude of the IMF. In such cases, the configuration of the magnetosphere changes as the usual shock-front between the kinetic solar wind and the geomagnetic field recedes, although the nature of the magnetosphere-ionosphere coupling is much less studied. Given a long enough period ($>$ 1 hour (Chané et al., 2015)) of sub-Alfvénic driving, Alfvén wings can form. Alfvén wings are tube-like structures, connected to the magnetic poles, that comprise of open magnetic field lines between the ionosphere and the solar wind (Neubauer, 1980). MHD simulations show that these can be thought of as the same structures that usually form the magnetotail lobes, although their angle is much greater with respect to the magnetospheric current sheet under sub-Alfvénic conditions (Ridley, 2007). Alfvén waves travel at the Alfvén velocity along IMF field lines that evolve under the influence of the solar wind plasma flow. The Alfvén waves and the resulting wings have an orientation that is dependent on that of the IMF, and the density and velocity of the solar wind, but the character of the plasma inside the structure is changed (Ridley, 2007). Under sub-Alfvénic conditions, the wings exhibit large angles to the flow of the solar wind plasma and disrupt the typical magnetospheric structure. Periods of low density, sub-Alfvénic solar wind are rare, with only 23 events with similar solar wind densities (where the minimum density $\rho < 0.3$ cm^{-3}; 11 of those being sub-Alfvénic) occurring between 1969 and 2003 (Usmanov et al., 2005). The mean duration of these sub-Alfvénic periods is $\sim$ 12 hours. Hajra and Tsurutani (2022) found 30 sub-Alfvénic events between 1992 and 2016, with a mean minimum M_A of 0.72. A recent occurrence of sub-Alfvénic solar wind flow at Earth, following the passage of an ICME, saw Alfvén wings formed. They were studied in detail with in-situ measurements, showing evidence of their direct magnetic connection with the solar surface, reconnection along the field lines of the wings and currents aligned with the wing structure, namely along the wing edges (Burkholder et al., 2024; Chen et al., 2024; Beedle et al., 2024).

$$M_A = \frac{v\sqrt{\rho_p \mu_0}}{B} \tag{1}$$

On 23 May 2002, the solar wind became close to sub-Alfvénic ($M_A \sim 1$) for over 24 hours, and was sub-Alfvénic for a number of hours, allowing Alfvén wings to develop.

The minimum M_A was exceptionally low, reaching $M_A \sim 0.4$. The event and the presence of the Alfvén wings was studied via in-situ measurements with the Geotail spacecraft, showing the changes in plasma parameters characteristic of a traversal of the wing (Chané et al., 2012). Given the northward orientation of the IMF for this period, the geomagnetic activity was expected to be very low and auroral activity suppressed, as is the case in general for periods of sub-Alfvénic solar wind flow. The transition between a super-Alfvénic and sub-Alfvénic solar wind has also been explored, providing context for the timescale of a transition from a magnetosphere with a bowshock and that with the Alfvén wings present (Chané et al., 2015). Due to its long duration ($\sim$ 24 hour) of very low density, sub-Alfvénic solar wind flow, this case provides a significantly long window of low M_A where the presence of Alfvén wings is certain and the magnetosphere exhibits the most complete configuration of the known events of this type. Although the auroral activity is expected to be suppressed under sub-Alfvénic conditions, this paper presents a new perspective on the magnetospheric configuration and coupling. This event was previously studied using observations from the IMAGE (Imager for Magnetopause-to-Aurora Global Exploration) spacecraft, where the Wideband Imaging Camera (WIC) (Mende et al., 2000) showed little auroral activity (Chané et al., 2012). Here, the narrow band spectrographic imagers (SI) (Mende, Heetderks, Frey, Stock, et al., 2000) of IMAGE are used to enhance the sensitivity to specific electron or proton precipitation and directly identify a UV auroral counterpart.

Section 2 introduces the primary data and observations used in the study. Section 3 then describes the observations, with an overview of the dynamics of the 23-25 May 2002 period providing context for a finer comparison of periods of super- and sub-Alfvénic solar wind driving of the magnetosphere and the corresponding auroral response. Section 4 then focuses on the possible inferences regarding the coupling that occurs in the inner magnetosphere.

2 Data and Instrumentation

This study uses remote measurements of auroral emission in the radio and UV wavelengths. The former uses instruments of both the Wind and IMAGE spacecraft, and are described further in Section 2.1. UV auroral emission is observed using only the IMAGE spacecraft, as described in Section 2.2. For context of the solar wind and geomagnetic conditions, we use in-situ measurements from the ACE spacecraft and the geomagnetic polar cap (PC) indices; described in Sections 2.3 and 2.4 respectively.

2.1 Radio Observations

The Wind/WAVES (Bougeret et al., 1995) and IMAGE/RPI (Reinisch et al., 2000) instruments measure surrounding radio emission across a similar range of frequencies, encompassing the typical AKR spectrum. In the case of Wind/WAVES, the signal amplitude is measured across a combination of dipole antennae at 32 distinct frequency channels between 20-1040 kHz and over a $\sim$ 3 minute period with a swept-frequency receiver. Here, observations are made using the $\sim$ 9 m Z antenna that is aligned with the spin axis of Wind. The data have been calibrated according to the method described in Waters, Jackman, et al. (2021) and normalised to a distance of 1 AU; spectral flux densities are given as 3-minute averages across a single receiver sweep. IMAGE/RPI uses an active Doppler radar technique to remote sense the local plasma environment, and measures between 3 kHz to 3 MHz, although here we display data only up to 1 MHz. The resolution of measurements varies along the spacecraft trajectory, and is between 13 s to $\sim$6 mins for the observations shown here. IMAGE/RPI data are provided by the combination of the four 250 m long X and Y antennae in the spacecraft spin plane.

2.2 UV Observations

The IMAGE/SI instrument measures wavelengths of auroral emission related specifically to proton and electron precipitation. Namely, the SI12 measures proton emission at 122 nm while the SI13 instrument measures electron emission at 136 nm (Mende, Heetderks, Frey, Lampton, et al., 2000). Both instruments have a wide field-of-view that allows imaging of the entire auroral oval when IMAGE is at apogee. This results in comprehensive spatial coverage of the polar region when combined with the highly elliptical orbit of IMAGE, which covers the northern hemisphere at perigee for the period considered here. For these three days, IMAGE performs 5 complete orbits with 9 hours of observations at 2 minute resolution.

The WIC instrument was used previously by Chané et al. (2012) to search for signatures of auroral emission and determine the extent of geomagnetic activity during this sub-Alfvénic event. In this study, we use the SI13 instrument to assess atmospheric aurora generated by electron precipitation and its relationship with AKR emission. Typical IMAGE/SI13 observations can include emission due to both solar photoionisation, known as dayglow and found on the dayside of the terminator, as well as a variety of auroral phenomena on both the dayside and the nightside including those related to precipitation from the cusp or directly from the magnetotail. Such phenomena are measured in the far UV range via emission of wavelengths between $\sim$ 120 nm and 190 nm, corresponding to spectral features that arise from proton and electron precipitation and subsequent excitation of neutral atmospheric constituents. The presence of these auroral components depends heavily on the interaction between the solar wind and IMF and the magnetosphere, namely from the plasma parameters of the solar wind and the orientation of the IMF. To explore the presence of such auroral components in the IMAGE/SI observations, the data are mapped to a regular magnetic coordinate grid which covers typical auroral magnetic latitudes. This mapping is described further in Section 3.1.

Each 2 minute integrated image is mapped to a local magnetic coordinate grid. The polar grid is centred on the northern magnetic pole and shows magnetic local time across 35-40 degrees of magnetic co-latitude, with grid cells covering 2×2 degrees. The mapped observations are visually examined over 20 minute periods and manually classified based on the presence of three main features. The first of these features are dominant dayglow emission without any clear auroral component, specifically when its presence affects the determination of distinct polar features, or other ambiguous features that prevent clear identification of or consistency with the polar spot. The second feature whose presence is evaluated is the electron polar spot itself, the novel auroral feature that is identified in this paper. Thirdly is the typical auroral oval emission found during typical solar wind-magnetosphere coupling. In the figures that follow (see e.g. Figure 1c), the first feature (dayglow/ambiguity) is represented by an orange rectangle, the second feature (distinct polar spot) is represented by a red rectangle and the third (oval) is represented by a blue rectangle. Auroral features are identified in this way due to the difficulty in isolating the true signal variability from that due to the changing instrument field of view, spacecraft position and general background variability due to dayglow. The spatially distinct nature of the polar auroral feature that is most relevant here warrants the use of visual identification. IMAGE/SI UV observations therefore appear in two forms in this article: magnetic polar mappings of the SI12 and SI13 observations and qualitatively-assessed presence of the auroral features mentioned above. While the full set of mapped observations from the 23 May to 25 May are too extensive to include in the manuscript, they can be found in Figure S4 of the supplementary information.

2.3 Solar Wind, IMF and Geomagnetic indices

In-situ observations of the solar wind and IMF are essential to monitor the upstream plasma conditions that impact Earth. In this study we use data from the ACE (Advanced

Composition Explorer) spacecraft for this purpose, as well as using plasma measurements to estimate the Alfvén Mach number. Magnetic field measurements are given by ACE/Magnetometer (MAG) (Smith et al., 1998) and the plasma density and velocity is obtained from the ACE/Solar Wind Electron, Proton and Alpha Monitor (SWEPAM) instrument (McComas et al., 1998).

2.4 PC indices

To quantify general geomagnetic activity and coupling with the solar wind, we use the PC indices (e.g. Troshichev & Andrezen, 1985; Stauning, 2013). The PC indices give a proxy for the flow of plasma across the polar cap via deflections from ground-based magnetometers found near the pole; positive values indicate flow towards the nightside, typically occurring under southward IMF Dungey cycle convection, while negative values indicate flow towards the dayside, during northward IMF and single- or dual-lobe reconnection processes.

3 Observational Evidence of Auroral Acceleration Processes

3.1 Sub-Alfvénic Solar Wind: Timeline

To summarise the context of the sub-Alfvénic period that is the focus of this study, Figure 1 shows an overview from 23 May to 25 May 2002, the same time period displayed in Figures 2 and 6 of Chané et al. (2012). The top two panels display Wind and IMAGE radio observations aimed at tracking bursts of AKR emission. The three bottom panels display the IMF components and the Alfvén Mach number measured upstream of the terrestrial magnetosphere, together with the PC indices measured at the magnetic poles.

Figure 1d shows the IMF components of the solar wind as measured by ACE. For 23 May, fluctuations in the IMF components represent a flux rope associated with the structure of an interplanetary coronal mass ejection (ICME) travelling towards Earth with a large magnetic field. Indeed, the low density solar wind is thought to be a consequence of the ICME expanding as the velocity of the ejecta, between the leading and trailing edge, decreased by 500 km.s^{-1} over 1.5 days (Chané et al., 2021). The IMF components decrease in magnitude for the remainder of 23 May. From 24 May, the components see little variation while the solar wind becomes rarefied; the IMF is northward ($B_Z \sim 2.5$ nT) with sunward ($B_X \sim$ -7.5 nT) and dawnward ($B_Y \sim 5$ nT) components. Figure 1e shows the Alfvén Mach number (M_A), calculated using equation 1. The data used for the calculation are from the ACE spacecraft and are described in section 2. We note that although the total mass density would be more ideal to calculate the Alfvén Mach number, as this would account for the potential presence of heavier ions in the solar wind, the previous *in-situ* observations of Alfvén wing structures and use of the ACE data in Chané et al. (2012) verify the sub-Alfvénic nature of the solar wind. The in-situ observations of the solar wind and IMF conditions are described in more detail in Chané et al. (2012, 2015).

Three distinct magnetospheric configurations, including that which exhibits Alfvén wings as explored by Chané et al. (2012), are shown by the labelled shaded regions present in the bottom four panels and by the dashed white lines in the top two panels. Interval I, between 11:00 UT 23 May and 00:00 UT 24 May, highlights activity under the normal, super-Alfvénic state of the magnetosphere, where the magnetopause forms a bowshock with the solar wind and the plasma circulation and FAC systems depend on single, dual or antiparallel reconnection processes with the IMF. Interval II, between 23:00 UT 24 May and 10:00 UT 25 May, indicates the period during which the solar wind conditions become sub-Alfvénic, such that the bowshock is expected to have receded, and Alfvén wings have been found to develop in this atypical open configuration of the magnetosphere. The period for which Geotail observed signatures of Alfvén wing structures

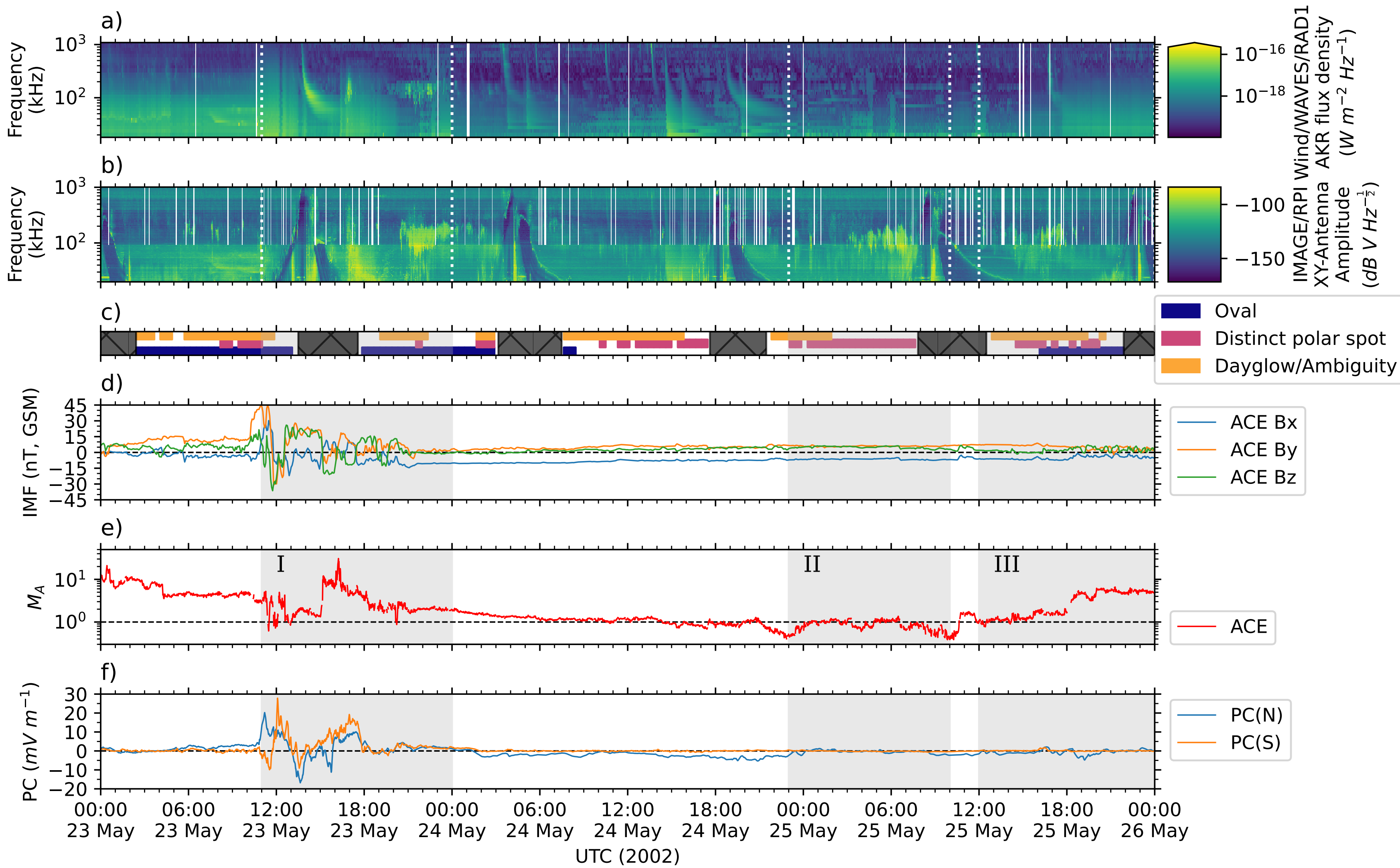

Figure 1. Timeline giving an overview of the solar wind and magnetospheric conditions from 23-25 May 2002. Panels a and b show frequency-time dynamic spectrograms from the Wind/WAVES and IMAGE/RPI instruments between 20 kHz and 1 MHz. Panel c illustrates the auroral features present in IMAGE/SI13 observations; black regions correspond to times when the instrument was not active and coloured rectangles on separate rows correspond to different auroral features (see text). Panel d shows the IMF components, in GSM coordinates, and panel e shows the Alfvén Mach number; both from the ACE spacecraft. Panel e is derived using equation 1. Panel f shows the PC indices for both the northern (PC(N)) and southern (PC(S)) hemispheres. The shaded regions in panels d-f represent periods of particular interest in this work, the first (I) pertaining to a super-Alfvénic magnetospheric structure with a bowshock present and typical coupling with the solar wind, the second (II) pertaining to the Earth under sub-Alfvénic solar wind conditions and that with highest confidence in the presence of Alfvén wings, and the third (III) pertaining to a transitionary period where the sub-Alfvénic magnetosphere again encounters usual, super-Alfvénic solar wind and sees the return of a bowshock.

in-situ, studied by Chané et al. (2012) and of explicit interest here, is between ∼16:00 UT 24 May and 17:00 UT 25 May. Interval III, between 12:00 UT 25 May and 00:00 UT 26 May, indicates a transitionary period from the sub-Alfvénic state to the typical configuration, where super-Alfvénic solar wind induces the reformation of the bowshock and reconnection at the dayside magnetopause is expected to resume.

The boundaries of these periods are chosen qualitatively based on solar wind parameters, the in-situ observations of Geotail, timescales for Alfvén wing formation from MHD simulations (Chané et al., 2012, 2015) and to best summarise the observations. Simulations of a linear transition over one hour from high density (5 cm^{-3}), super-Alfvénic to low density (0.04 cm^{-3}), sub-Alfvénic solar wind indicate the formation of Alfvén wings beginning a few minutes after the lowest density solar wind reaches the magnetosphere. The wings develop fully after $\sim$ 1 hour (Chané et al., 2015). As mentioned in their study, the simulated decrease in solar wind density occurs over a much shorter timescale than that observed, which occurs non-linearly over an almost 24 hour period as shown by the Alfvén Mach number in Figure 1e. The timescale for Alfvén wing formation is therefore expected to differ. Calculations using the median solar wind speed of 500 km s^{-1} (from ACE) during sub-Alfvénic conditions give a timescale of approximately 1 hour for the solar wind to reach Earth. Given that the magnetosphere was embedded in low density ($<$ 1 cm^{-3}) solar wind for ∼26 hours before the first significant period of sub-Alfvénic solar wind (from 18:00 UT 23 May to 21:00 UT 24 May), the bowshock would already be weakened and receded and thus the conditions for Alfvén wing formation could already exist. For this reason the formation timescale is expected to be shorter for the observed decrease in solar wind density than in the simulations. However, to be conservative in the assumption that the Alfvén wings are present, the period of interest (II in Figure 1) related to these dynamics is restricted. Since the solar wind has been sub-Alfvénic, and decreasing, for 3 hours prior to the start of interval II we assume that the Alfvén wings are established. The periods and their accompanying observations as related to this study are described explicitly between Sections 3.2 and 3.4.

Figures 1a and 1b show frequency-time dynamic spectrograms of radio observations from the Wind/WAVES and IMAGE/RPI instruments. The Wind spacecraft, at a radial distance of $\sim$ 300 Earth radii ($R_E = 6371$ km) and located on the dayside for the entirety of the period displayed in Figure 1, exhibits solar Type III radio bursts (eg 14:00 UT 23 May) and faint AKR emission corresponding to interval I (around 17:00 UT and between $\sim$ 19:30 UT 23 May - 00:00 UT 24 May). No AKR counterpart was detected by Wind/WAVES during intervals II and III. The remote, dayside viewing position of Wind is unfavourable for observing typical AKR bursts that are produced by sources on the nightside, due to the anisotropic emission patterns of AKR sources. Using a multipoint observation with both Wind and IMAGE therefore gives a more complete perspective of the AKR occurrence across the magnetosphere.

Due to the upstream location of Wind, emission below ∼50 kHz probes the local solar wind plasma density, since Langmuir waves at the plasma frequency and quasi-thermal noise dominate the spectrum in general. Figure 1a shows this with the decrease in intensity at low frequencies between 00:00 UT 24 May and ∼18:00 UT 25 May, coinciding with interval II. The IMAGE spacecraft is within a radial distance of 7 R_E of Earth for the period here, and follows a highly elliptical, $\sim$ 16 hour long, polar orbit with apogee above the northern hemisphere. IMAGE is therefore ideal to complement the radio observations of AKR from Wind with another, more time-variable observing location. Characteristic plasma waves are seen in the IMAGE/RPI spectrograms when the spacecraft passes the magnetic equator at perigee, such as between 12:00-16:00 UT 23 May, coming close to the plasmasphere where the plasma density and therefore plasma frequency increases and external radio emission is blocked. AKR is observed clearly between 19:30 UT 23 May and 00:00 UT 24 May, during interval I. Additional AKR bursts, not observed by Wind, were also detected between 23:00 UT 24 May and 00:00 UT 26 May (corresponding to intervals II and III). Interestingly, the amplitude, spectrum and duration of these three bursts are relatively comparable. The general increase in amplitude below $\sim$ 100 kHz for the entire 3 day period is an instrumental effect due to an increase in gain at the receiver level relative to higher frequencies. Figure 1c shows the UV auroral features that are present in the observations of IMAGE/SI12 and IMAGE/SI13, as determined by visual examination of the full set of mapped observations (see Section 2.2 for a description of the mapping).

Figure 1f shows the PC indices for the three day period. Both sunward and anti-sunward flow is seen for interval I, with magnetic flux opening at the subsolar magnetopause and at higher magnetic latitudes as the IMF changes orientation. From 24 May, the PC indices decrease significantly. This corroborates the findings of Chané et al. (2012) in that there was little geomagnetic activity for the sub-Alfvénic period, however it must be noted that these indices capture a limited aspect of expected ionospheric activity; the auroral dynamics along the oval are not well sampled, for example. To explore the inner magnetospheric coupling and activity more closely, the following sections provide a more detailed description of the periods of note.

3.2 Auroral Observations During Super-Alfvénic Conditions

Figure 2 shows radio and UV auroral observations used here to identify the auroral acceleration processes at work during interval I. Figure 2e shows the Alfvén Mach number at the ACE spacecraft decreasing non-linearly from a typical magnitude, around 15:00 UT, to $M_A \sim 2$ from $\sim$ 21:30 UT as the plasma density of the solar wind decreases. This is persistent until the end of the day. During this interval, the magnetosphere exhibits a bowshock and magnetosheath structure on the dayside and magnetic reconnection between planetary and IMF can occur at the magnetopause (near the subsolar point when $B_Z < 0$). The first three panels correspond to those shown in figure 1: figures 2a and 2b show radio observations from Wind/WAVES and IMAGE/RPI, while figure 2c illustrates the auroral features present in IMAGE/SI13 observations, visually classified as described above. Figure 2d shows examples of pairs of observations from IMAGE/SI12 (proton emission, blue) and IMAGE/SI13 (electron emission, red) that best illustrate the auroral components for this period. The observations have been processed as described in Section 2.2, being gridded to a magnetic coordinate system after integrating over a 2 minute window. Each SI12 and SI13 image is shown with 12 hours MLT (noon) at the top, 24 hours MLT (midnight) at the bottom and 6 hours MLT (dawn) on the right. The arrows highlight the specific time of each example in the panels above and below, which is indicated with a dotted, vertical black line. Figure 2e shows the Alfvén Mach number from the ACE spacecraft as in Figure 1e.

Figures 2a and 2b show the AKR measurements, which are typical in morphology, observed during typical coupling between the solar wind and the magnetosphere, namely between 20:30-23:00 UT 23 May. Other radio features are present, such as a solar radio Type III burst observed by Wind/WAVES between 13:40 and 16:00 UT and the attenuation of radio signal due to the traversal of the dense plasmasphere by IMAGE/RPI between $\sim$ 12:00-16:00 UT. Given the large positional discrepancy of the two spacecraft, the time-frequency structure of the AKR bursts remain similar, particularly in the general spectral range. Looking more closely it is clear that the variability of the AKR intensity observed by Wind does not correspond exactly to IMAGE observations, but since the latter are not calibrated a direct comparison between spacecraft is not straightforward. The general similarities suggest that both spacecraft were observing a common region of AKR sources colocated with longitudinally extended aurora following the compression of the magnetosphere and the intensification of auroral electrojets. This is corroborated by the general temporal correlation, similarities in spectral extent and its variability, and the auroral oval morphology as indicated in figures 2c and d. Notably, and most clearly seen by IMAGE/RPI for the spectrum of the AKR burst beginning at $\sim$20:30 UT,

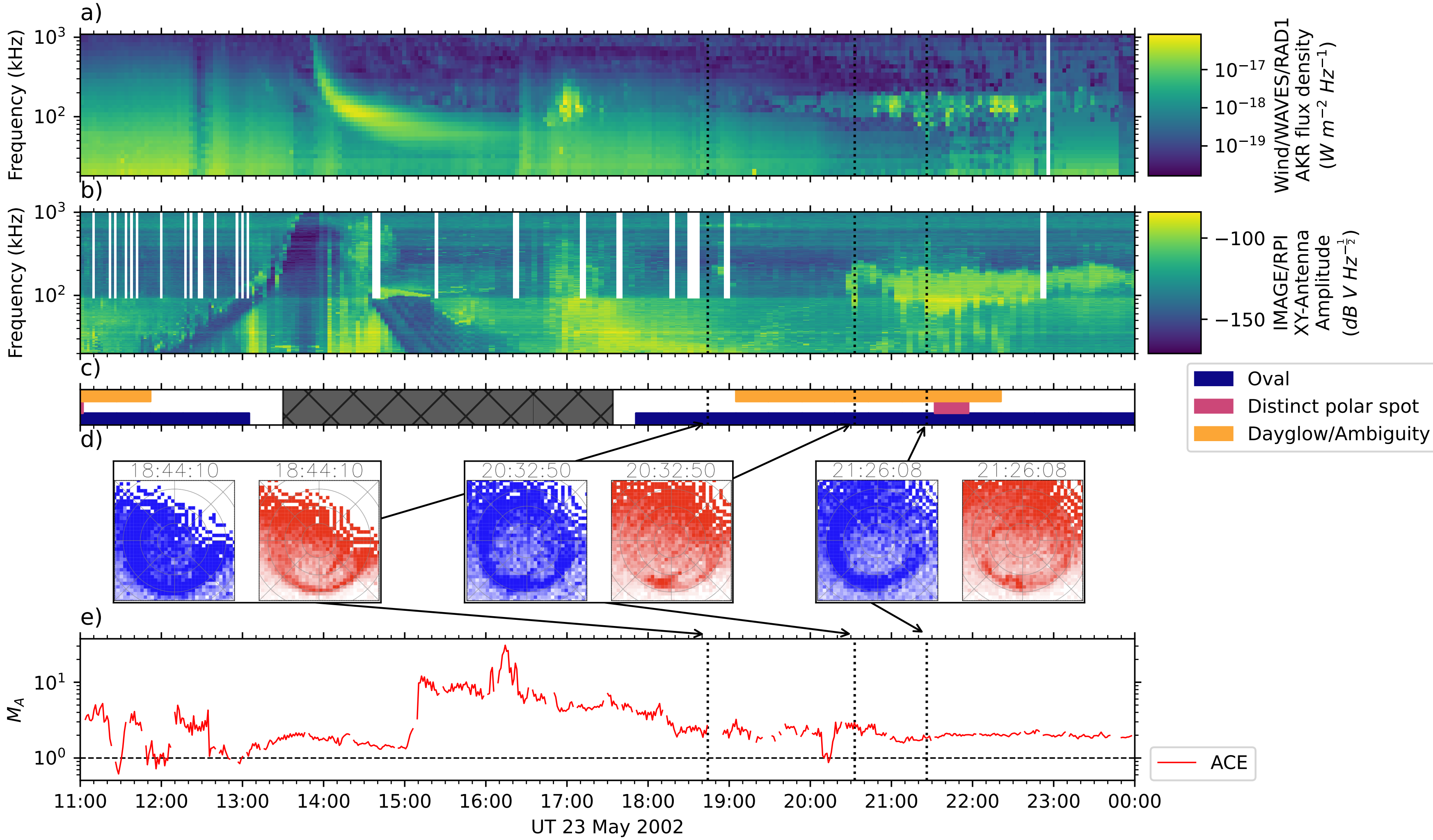

Figure 2. Radio and UV auroral observations with the solar wind Alfvén Mach number showing interval I of Figure 1. Panels a and b are as shown in Figures 1a and 1b. Panel c shows the auroral features as visually identifed from magnetically gridded IMAGE/SI observations, as described in Section 3.1. Panel d shows exemplary 2 minute integrated IMAGE/SI12 and IMAGE/SI13 observations that characterise the period, mapped onto a magnetic coordinate grid of magnetic latitudes above ∼55°, with 24 hours MLT shown on the bottom of the plot and 12 hours MLT at the top. For each snapshot, proton UV emission is shown on the left in blue, while electron UV emission is shown on the right in blue with the corresponding time of integration shown above and arrows showing the corresponding times in the panels above and below. Panel d shows the Alfvén Mach number as shown in Figure 1.

there is an extension to lower frequencies over the following hour. The calibrated AKR observations by Wind/WAVES show a peak spectral flux density of $\sim 10^{-16}$ Wm^{2}Hz^{-1}, while IMAGE/RPI observes AKR bursts at receiver intensities of ~ -90 dB. Given the above inference of common, bulk AKR sources, this provides a qualitative baseline for which to compare other AKR observations from this period.

Figure 2c shows a persistent auroral oval, with apparent activity at pre-midnight MLT ($\sim$ 23:00 hours MLT) after 20:30 UT that likely indicate substorm dynamics. The dominant feature for this period is the well-known oval structure shown via both proton and electron UV aurora, with brightenings occurring in the electron aurora due to substorm activity and some transpolar arc-like structures. Examples of these are seen particularly in the IMAGE/SI13 observation at 18:44:10 UT (transpolar arc) and 20:32:50 UT (substorm). Substorm event lists based on the SuperMAG SML index (Gjerloev, 2012) and global auroral images (Frey et al., 2004) show events for 23 May, with agreement on a substorm onset occurrence around 20:20 UT (Newell & Gjerloev, 2011; Forsyth et al., 2015). Substorm onsets are also identified around 17:00 UT (Frey et al., 2004; Newell & Gjerloev, 2011; Forsyth et al., 2015), around the time of the first AKR burst observed by Wind/WAVES in interval 1 (see Figure 2a); highlighting the usefulness of typical super-Alfvénic AKR as one of the indicators of substorm onset. In particular, the decrease in frequency of the AKR bursts are akin to low frequency extensions, representing the extension of the auroral acceleration region to higher altitudes; a well observed phenomenon at substorm onset (Morioka et al., 2007; Waters et al., 2022). Complete IMAGE/SI observations are not available until $\sim$17:30 UT on 23 May. The SuperMAG indices themselves show enhanced SML, with sharp decreases highlighting intensifications of the westward electrojet and substorm onset. The SMU index is also significantly enhanced, suggesting general energisation of the magnetosphere and convection. Such dynamics are represented in part by the auroral brightening around midnight (examples in Figure 2c at 20:32:50 UT and 21:26:08 UT). This follows plasma transport across the polar cap, as indicated in the PC indices of shaded region I in Figure 1f. Once in the magnetotail, plasma contributes to the equatorial ring current and can also strengthen FACs, entering the nightside ionosphere at high magnetic latitudes following reconnection in the magnetotail. The location of bright aurorae can be used to assess the approximate location of AKR sources (assuming that the other generation conditions are met, such as the existence of a plasma cavity which requires sufficient acceleration), given the colocation of discrete aurora and AKR sources (Menietti et al., 2011). Discrete aurora and AKR is better observed by IMAGE, situated approximately above the magnetic pole, compared to the location of Wind, 300 R_E on the dayside.

3.3 Auroral Observations During Sub-Alfvénic Conditions

Figure 3 corresponds to interval II of Figure 1, and has the same panel layout as figure 2. As shown in Figure 3e, the Alfvén Mach number is $\lesssim 1$ for the period. A timescale of $\sim$1 hour is expected for the majority of closed geomagnetic field lines to open into Alfvén wings once sub-Alfvénic solar wind reaches the magnetosphere (Chané et al., 2015). Following this, and an extended period of sub-Alfvénic solar wind reaching Earth, any short, minor deviation from sub-Alfvénic solar wind will not immediately reinstate a bowshock and the super-Alfvénic magnetosphere configuration. Instead, a non-ideal Alfvén wing configuration may persist (Chané et al., 2012). The configuration throughout the period shown in Figure 3 is therefore expected to remain dominated by the Alfvén wing structure.

For the 11 hours of observations here, Wind/WAVES observes much fainter AKR emission overall in Figure 3a than in Figure 2a. At frequencies $\gtrsim 100$ kHz, faint, spurious emission is observed mostly from solar Type III radio bursts and storms. The IMAGE/RPI observations in Figure 3b show similar features to that seen in Figure 2b. In general, the AKR bursts observed by IMAGE are similar in intensity and spectral range

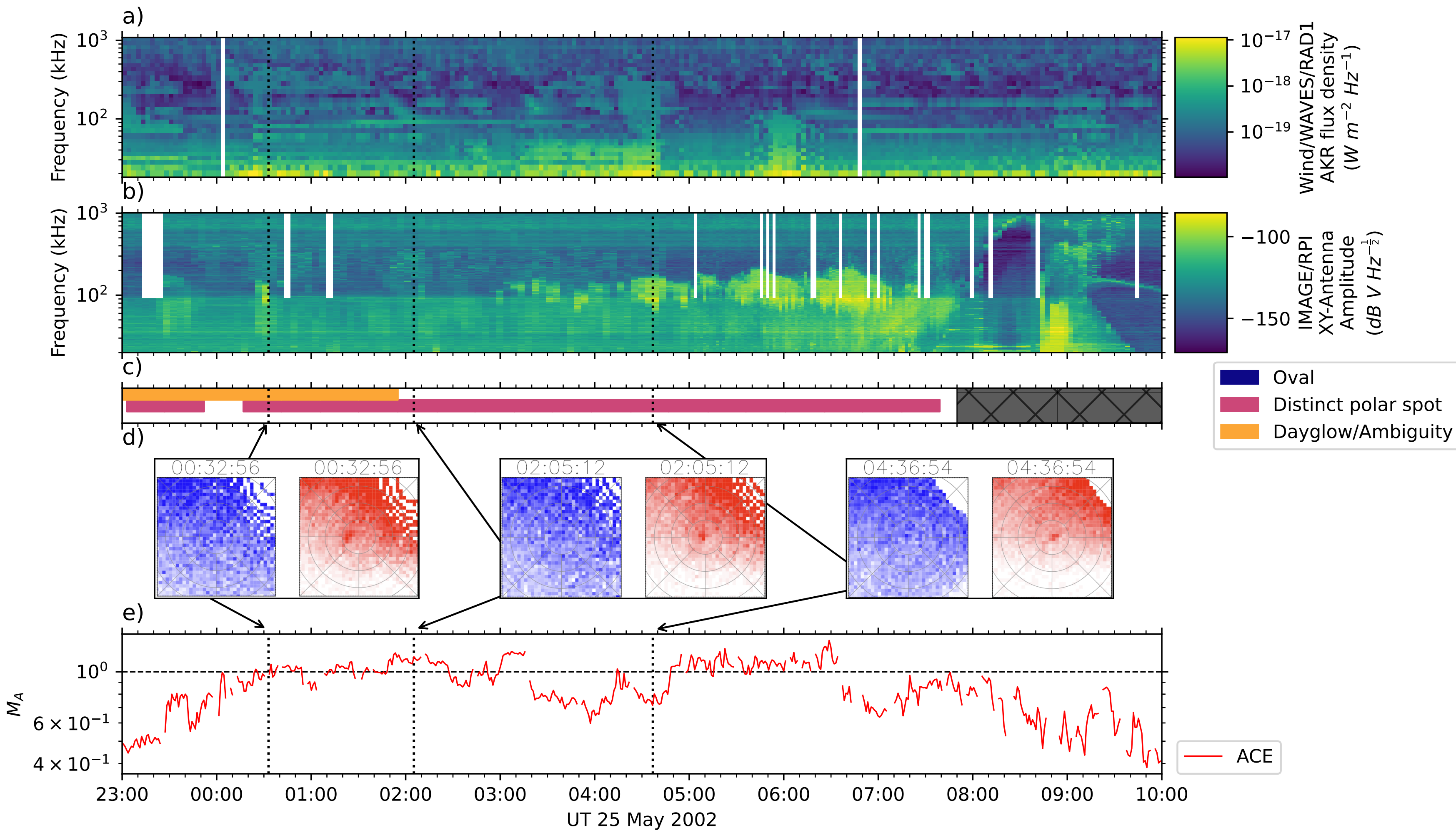

Figure 3. Radio and UV auroral observations with the solar wind Alfvén Mach number, as shown in Figure 2, here pertaining to interval II of Figure 1.

to those observed by IMAGE in interval I during super-Alfvénic conditions (Figure 2b), exhibiting receiver intensities between -100 and -90 dB. Wind/WAVES observes faint emission that temporally correlates to some of this emission, such as that between 04:00 UT and 05:00 UT. The larger discrepancy in observed intensity between the two spacecraft suggests that there is a visibility effect present in this interval II compared to interval I, therefore suggesting an uncommon source locus.

Emission is observed by IMAGE/RPI at 100 kHz, a typical AKR frequency, around 00:30 UT 25 May; limited in spectrum and with a short duration. Following this, a longer period of emission is observed from 03:00 UT that varies in spectrum quasi-periodically ($\sim$ 1 hour period). This latter period of emission gradually covers an increasing range of frequencies, indicating an increase in extent of the accelerating region. Here however, the region extends to lower altitudes. The emission is seen at 100 kHz from 03:00 UT, exhibiting a spectral range typical of AKR. The spectrum increases in extent to between 60-200 kHz by 07:00 UT before the spacecraft approaches perigee and the radio signal is cut off once more by the plasmasphere. This is indicative that the AKR amplification is as efficient as that seen in interval I.

Figures 3c and d show the presence of a novel auroral feature driven only by electron precipitation. The red rectangle indicates the persistence of this feature in the IMAGE/SI13 observations; a localised patch of UV electron aurora (hereafter referred to as the polar spot) is surprisingly seen at the magnetic pole, at magnetic latitudes $> 80°$ and often $> 88°$. It covers a square grid of between 2-4 cells, corresponding to a square of between 4°-8° latitude. This emission is distinct from the dayglow, and in this example corresponds with the lowest Alfvén Mach number value ($M_A \sim 0.4$), although the polar spot is already observed prior to the arrival of sub-Alfvénic solar wind (figure 1c between $\sim$ 10:00 UT and 18:00 UT 24 May). This prior presence of the polar spot is observed while the solar wind has abnormally low density, but not yet sub-Alfvénic, and indicates that auroral precipitation persisted both as the Alfvén wings are established and whilst they are at their most complete.

The three examples of conjugate IMAGE/SI12 and SI13 observations shown in figure 3 show the polar auroral spot at distinct times. The first of these aligns with the brief period of AKR emission at 100 kHz. No bright AKR signature is seen with the following example at 02:05 UT. The latter example aligns with the longer duration AKR emission. As again indicated by Figure 3c, the polar auroral spot is present for all IMAGE/SI13 observations made here. There is variability in the intensity and spatial extent, but the feature remains distinct and within $< \sim 10°$ of the pole. Figure 4 shows $\sim$ 20 minutes of IMAGE/SI observations between 06:33 and 06:57 UT on 25 May for further clarity of the morphology and consistency of the polar spot. These are mapped in the same way to those in Figure 3d. All mapped IMAGE/SI observations can be browsed in Figure S4 of the supplementary information.

Based on these IMAGE/SI13 observations, the aurora take the form of a polar, long-lasting, isolated and spatially constrained spot. Any other auroral components, such as the auroral oval prevailing during interval I, have vanished. Given this, and the general temporal correlation with the AKR observed by IMAGE/RPI, we infer that the source electrons of the UV emission and the AKR source region are colocated along magnetic field lines roughly centred at the magnetic pole. However, the time variability in the AKR indicates that the growth rate becomes sufficient to amplify AKR only for specific periods. This implies that although the conditions for the instability are present intermittently, the electron acceleration is significant enough to sustain AKR generation.

3.4 Return of Super-Alfvénic Conditions

Figure 5 shows radio, UV and Alfvén Mach number observations for the latter shaded region (III) of Figure 1. Here, the solar wind becomes super-Alfvénic at $\sim$ 14:00 UT. The

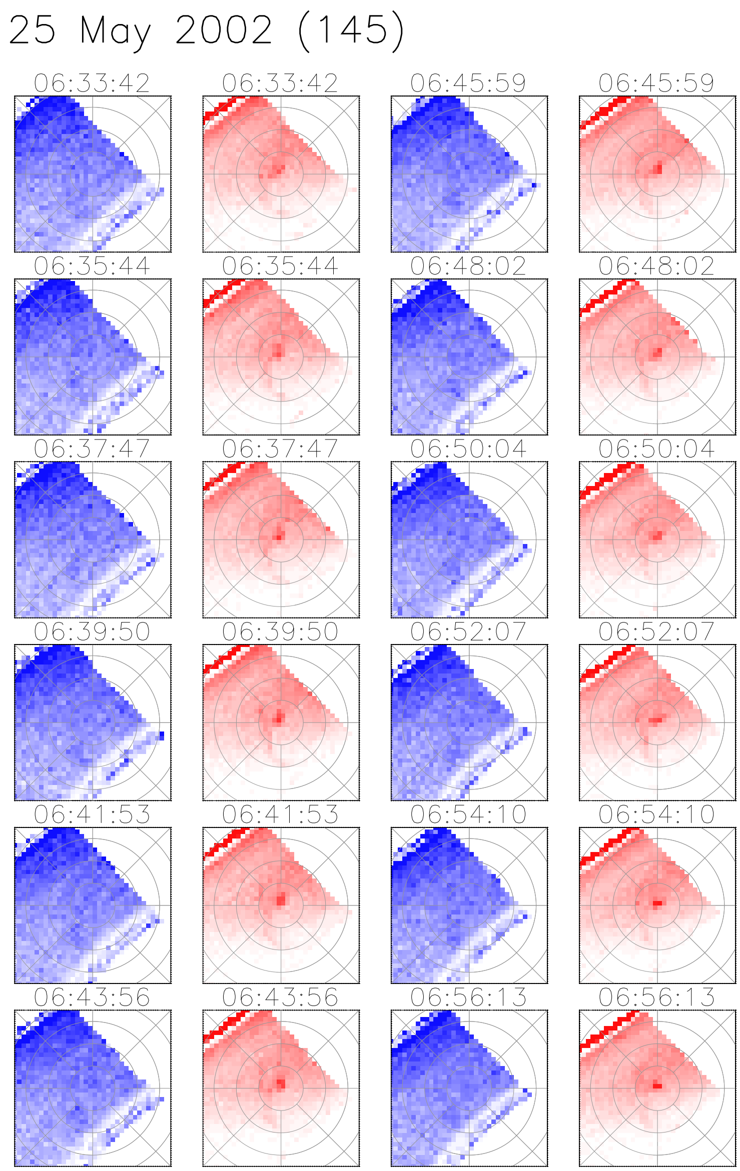

Figure 4. Examples of mapped IMAGE/SI observations between 06:33 UT and 06:56 UT 25 May 2002 that display the polar electron auroral spot. Each pair of maps for a given UT, displayed above each observation, shows IMAGE/SI12 (proton) observations in blue and IMAGE/SI13 (electron) observations in red. Examples are integrated over $\sim$ 2 minutes and are shown chronologically reading from the top to bottom of first the left and then the right columns.

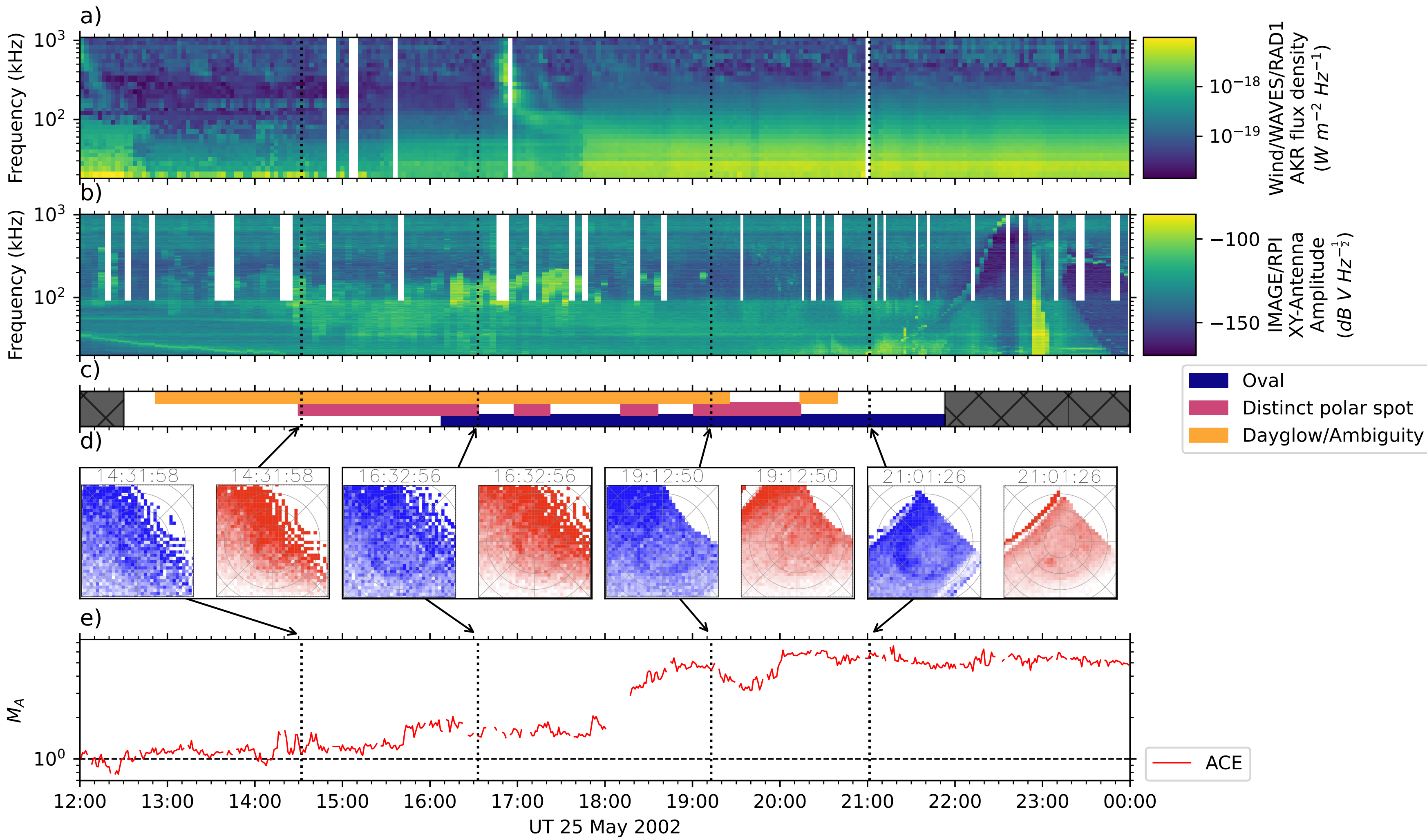

Figure 5. Radio and UV auroral observations with the solar wind Alfvén Mach number, as shown in Figure 2, here pertaining to interval III of Figure 1.

Alfvén Mach number continues to increase in a step-like manner, reaching M_A ~2 at 16:40 UT and M_A ~4-5 at ~ 18:30 UT. Once the more dense, super-Alfvénic solar wind reaches Earth, the bowshock will return the magnetosphere to its usual configuration and standard auroral precipitation along the main oval will occur. While the exact dynamics and timescale of this transitionary period are not examined in detail here, it is likely that some combination of morphologies drive the electron acceleration for this period; of that during the presence of Alfvén wings and those of the typical coupling that preceded their formation.

Figure 5a again shows the Wind/WAVES dynamic spectrogram, without any clear AKR emission. The primary features for these observations comprise an intense Type III burst around 16:40 UT 25 May and a sharp intensification of emission below 100-200 kHz after 17:40 UT. As mentioned in Section 3.1, the low frequency intensification is due to an increase in the plasma (solar wind) density local to Wind. For the orbit of IMAGE and the subsequent RPI observations shown in 5b, AKR emission is seen between ~ 16:10 and 18:00 UT with further temporal correlation with the auroral polar spot. The first instance of super-Alfvénic solar wind would be expected to reach Earth after ~ 1 hour, at ~ 15:00 UT. For occasions of low magnetospheric driving (satisfied here due to the low IMF magnitude and weakly northward B_Z component) under super-Alfvénic solar wind flow; Browett et al. (2017) find a timescale of 3-5 hours for IMF field lines reconnecting on the dayside magnetopause to reach the plasma sheet in the magnetotail. Thus the plasma carried with the newly opened field lines would only be able to enter the ionosphere after this delay. Ignoring the timescale for reformation of the bowshock we would thus expect any typical auroral emissions to return after ~ 18:00 UT at the earliest. The AKR observed by IMAGE/RPI in Figure 5 is therefore inferred to be emitted from a similar source region to that during the Alfvén wing configuration, and likely due to the same mechanism. The auroral components present in the IMAGE/SI observations are mixed and more difficult to define clearly, with an oval appearing in proton aurora observations, as well as localised electron aurora that is less spatially constrained as the examples in figure 3.

3.5 Observational evidence of upward FACs

To explore the nature of the acceleration processes responsible for the electron UV emission and AKR observations, we examined observations of ionospheric plasma flow and convection from Super Dual Auroral Radar Network (SuperDARN) and the Defense Meteorological Satellite Program (DMSP) spacecraft. SuperDARN uses doppler-shifted backscatter radar measurements to determine plasma flow velocity vectors within the ionosphere. DMSP are a constellation of polar-orbiting spacecraft that carry a host of instruments able to probe the ionosphere; here we utilise mostly the Topside Ionospheric Plasma Monitor (SSIES). DMSP/SSIES measures ion trajectories in the direction perpendicular to the spacecraft trajectory (cross-track) across the auroral zone and polar cap. This acts as a proxy for the plasma flow and thus can also explore the presence of an appropriate convection cell to host an upward FAC. These observations thus provide context for the UV and radio auroral measurements shown in the previous Sections. Unfortunately, more direct measurements of FACs from the Active Magnetosphere and Planetary Electrodynamics Response Experiment (AMPERE) (B. J. Anderson et al., 2000, 2014) are not available for 2002.

SuperDARN observations show the presence of a large, clockwise-rotating convection cell above the location of the magnetic pole. These observations occur whilst the electron polar spot is active, and such a convection cell could host an upward FAC. The observed plasma flow vectors required for fitting the cell are sparse at times; often no, or very few, vectors are present at all. For a few integration periods there are sufficient numbers of vectors, however. Examples of these are shown in Figure S1 of the supplementary information. Each DMSP spacecraft completes a pass of the polar magnetosphere of a given hemisphere in approximately 20 minutes. DMSP/SSIES cross-track trajectories at 23:30 UT 24 May and 00:51 UT 25 May indicate the existence of a clockwise-rotating convection cell above the magnetic pole in the northern hemisphere. With the Special Sensor for Precipitating Particles (SSJ) instrument, DMSP is also able to make electron flux measurements that coincides with the SSIES cross-track trajectories observed during an orbital pass. These observations show increased electron flux for both 23:30 UT 24 May and particularly 00:51 UT 25 May at energies of a few keV, which coincide roughly with what we interpret as the signature of the clockwise-rotating cell in the DMSP/SSIES observations. Such electron energies are in the range to provide conditions for AKR generation (Ergun et al., 2000). Other ion trajectories from DMSP/SSIES suggest two convection cell patterns present in the northern hemisphere, with the strongest signatures at 13:25 UT, 15:06 UT and 20:08 UT on the 24 May. At 16:46 UT and 18:28 UT on 24 May, prior to the arrival of sub-Alfvénic solar wind but $\sim$ 10 hours after solar wind with an Alfvén Mach number of M_A $\sim$1 has arrived at Earth, the ion flows also exhibit what could be a single clockwise-rotating convection cell centred on the pole. The aforementioned DMSP/SSIES observations are shown, with cross-track ion velocities projected onto a magnetic polar map, in Figure S2 of the supplementary information. DMSP/SSJ observations of electron flux corresponding to possible single convection cell patterns at the pole at the start of interval II can be found in Figure S3 of the supplementary information

4 Discussion

4.1 Morphology of Auroral Acceleration and Emission

The sub-Alfvénic event of 24-25 May 2002 exhibits previously unexplored auroral dynamics in both the UV and radio wavelengths. As recently observed by (Beedle et al., 2024), the Alfvén wing configuration of the magnetosphere under sub-Alfvénic solar wind driving can support auroral acceleration and emission processes which here have been observed via the auroral emission itself. Such dynamics are localised, constrained to the magnetic pole, and show electron acceleration enough to sustain AKR emission similar to that exhibited during super-Alfvénic magnetospheric configurations. IMAGE/SI13 observations show evidence of a electron aurora within a few degrees of the magnetic pole in the northern hemisphere. Multipoint observations of AKR with Wind/WAVES and IMAGE/RPI suggest a localised flux tube as the source, when considering the discrepancies in viewing position and observations. The auroral observations and the resulting inferences are discussed here; interval I of Figure 1 exhibits observations during super-Alfvénic driving of the magnetosphere. Typical features are present, namely a bright auroral oval with both proton and electron aurora and widely observable AKR bursts from longitudinally distributed sources. AKR bursts and characteristic low frequency extensions of the spectrum occur around the time of catalogued substorm onsets from multiple event lists. Interval II, which begins after the magnetosphere has been subject to sub-Alfvénic solar wind, is completely dominated by the highly localised electron auroral component that is found centred on the magnetic pole. Some time periods are often contaminated by enough dayglow to prevent a clear determination of this feature, however. Based on this and the simultaneous multipoint AKR observations, there appears to be significant electron acceleration while the magnetosphere is characterised by the Alfvén wings. Interval III represents a transitionary period, and is characterised by a mix of the auroral components used here; a faint auroral oval is present and the polar spot continues to emit, although it is less constrained to the pole.

During interval I, under super-Alfvénic driving, both Wind and IMAGE observe AKR bursts that are comparable in both spectral and temporal characteristics. Given that the IMAGE observations during interval II show AKR bursts with a similar intensity to those observed during in interval I, this implies that the ECMI mechanism that generates AKR is as efficient during the sub-Alfvénic than the super-Alfvénic configuration. Necessarily, this further implies that a population of electrons have been accelerated to produce AKR. As well as this, there is less correspondence between the Wind/WAVES and IMAGE/RPI observations of interval II, with the former being fainter. This is not the case for interval I, and indicates the spatial extent of the flux tube footprint that hosts the AKR source region. Given that the AKR beaming is directed in a hollow cone at large angles to the magnetic field, the fact that Wind observes weaker AKR indicates that active sources are constrained to a different, localised region of magnetic flux in comparison to the super-Alfvénic period, where AKR sources are longitudinally distributed about the auroral oval. Interestingly, contrary to the typical AKR behaviour at substorm onset, the AKR bursts observed by IMAGE/RPI during interval II imply that the auroral acceleration region extends to lower altitudes after continued driving of the polar spot. While exploring possible locations of AKR sources based on beaming patterns is out of the scope of this study, this further supports the hypothesis of a spatially constrained source region. It is also possible that the IMAGE spacecraft moves in and out of the illumination region of such a source region throughout the period, which would imply that the radio variability could be due to the changing orientation of the northern Alfvén wing.

The conjugate observations of the constrained electron UV aurora with the multipoint AKR observations imply the footpoint of the active auroral acceleration region through which the inner and outer magnetosphere are coupled. Chané et al. (2015) show the simulated magnetic field morphology of a sub-Alfvénic magnetosphere under similar conditions, with symmetrical dipolar closed field lines and open field lines along the Alfvén wing. Given the northward IMF conditions prior to the arrival of sub-Alfvénic solar wind, the open flux in the magnetosphere is likely to have been reduced (Fairfield et al., 1996; Song et al., 1999; Milan et al., 2022). If the Alfvén wings were to support an upward FAC, it would flow along open field lines that would then be highly localised, and near the magnetic pole. The Alfvén wings of the Jovian satellite Io sustain an Alfvénic current via a convection electric field driven by its motion in the Jovian magnetosphere (Neubauer, 1998; Chust et al., 2005). Such currents have been observed with the presence of Alfvén wings at Earth recently, and as such are plausible to be responsible for the electron acceleration here (Beedle et al., 2024). Although the northward component of the IMF is quite weak ($\leq$ 5 nT) here, it is possible that dual-lobe reconnection occurs and, if the auroral oval is significantly contracted, could cover the polar region in discrete aurora (Y. Zhang et al., 2009). However, it is not clear how the opening of flux in the polar cap that subsequently forms the Alfvén wings would modify this scenario (Chané et al., 2015; Chen et al., 2024).

The examples of IMAGE/SI12 and SI13 observations in Figure 5 also indicate the return of typical auroral morphology and magnetospheric structure; the return of a faint auroral oval from both proton and electron precipitation is seen, particularly in the example at 16:32 UT. AKR is observed at this time, and so the aforementioned point regarding timescales of typical coupling is refuted somewhat. However, if the diffuse auroral oval arises from the re-establishment of a ring current structure leading to weak electron precipitation, it could be assumed that the predominant acceleration processes are those due to the Alfvén wing configuration. Although ambiguous in some cases, the polar auroral spot is sustained during this period, and the discrepancy between Wind and IMAGE radio observations still exists. Note that the example of Figure 5d at 21:01 UT shows a localised electron aurora, but it is then found towards dusk/night MLTs. It is plausible that the acceleration processes established under the Alfvén wing configuration continue to be responsible for the AKR emission here as IMF conditions change.

4.2 High-Latitude Dayside Aurora

The preceding solar wind conditions as the sub-Alfvénic solar wind arrives at Earth and the characteristics of the auroral emission are consistent with a specific class of aurora, usually found on the dayside under an NBZ current system (i.e that established when the IMF is northward) (Frey et al., 2003; Carter et al., 2018), that is known as HiLDA. Other authors have previously identified the period studied here as likely to exhibit HiLDA (see Figure 3 of Frey et al. (2004)), although the exact response of the inner magnetosphere in this case was not explored explicitly. That the electron aurora is consistently centred at the magnetic pole is contrary to the expected HiLDA paradigm.

Given the solar wind and IMF conditions from 24 May (see Figures 1 and 3), and the observational evidence from DMSP/SSIES, it is likely that an NBZ current system related to HiLDA is established (Frey et al., 2004). As the sub-Alfvénic solar wind reaches Earth and the Alfvén wings begin to be formed, this current system is expected to be modified. As mentioned previously, the IMF B_z component turns northward from approximately the beginning of 24 May 2002, as the solar wind density and Alfvén Mach number also begin to decrease. The observed changes in the IMF components and the drop in solar wind density are statistically favourable conditions for the generation of HiLDA emission (Frey et al., 2004). Northward IMF creates reconnection sites near the cusp, generating a downward FAC and strengthening the region 0 current system, where two potential cells of sunward convection are established (Milan et al., 2017; Frey et al., 2019). When there is a significant B_Y component to the IMF, the location of the FAC and convection cells change; for strong positive B_Y, the convection cells are rotated such that the clockwise-rotating cell becomes centred on the noon-midnight meridian. This clockwise convection cell hosts the upward FAC which sees electrons enter the magnetosphere from the solar wind. As the solar wind density drops and positively charged current carriers are diminished, a parallel electric field is set up that accelerates electrons into the ionosphere, maintaining the upward FAC of the previously established current system (Frey, 2007; Frey et al., 2019). The highly conducting ionosphere in the northern hemisphere, due to the high photoionisation of the summer months, is able to maintain continuity via the flow of ionospheric Pedersen currents. The inner magnetospheric dynamics described above are confirmed for both northern and southern hemispheres (Carter et al., 2018; Frey et al., 2019).

Convection cells are highly responsive to solar wind driving as previously mentioned; southward and northward IMF both produce vastly different convection patterns which are further modified by other IMF components, namely duskward and dawnward (B_y) components, and such patterns and their loci can be mobile (Walach et al., 2022). In a study of reconnection processes during a recent occurrence of sub-Alfvénic driving, Burkholder et al. (2024) find that magnetotail reconnection can continue to take place (as was also predicted by Chané et al. (2015)) and that the preceding magnetospheric dynamics could be sustained. While the polar auroral feature is present from the IMAGE observations during the earlier parts of 24 May 2002, no AKR was observed. This does not rule out the same system for the later production of AKR however; the presence of electron UV aurora does not necessarily imply a growth rate sufficient for AKR generation. The visibility of the AKR emission for a remote observer could also be limited if the position of the source or spacecraft changes significantly. The presence of AKR at later times, with intensity as observed in Figure 1 for example, does indicate similar AKR characteristics to that produced in the super-Alfvénic period.

Space hurricanes are a phenomenon related to HiLDA, so called due to the large convection cell that is generated above the magnetic pole, instead of the typical location of the NBZ current system (Carter et al., 2018). Under northward IMF, a dominant IMF B_Y component can produce reconnection poleward of the cusp at high latitudes (Q. H. Zhang et al., 2021). Due to the B_Y component, the newly opened field lines are draped in a circular path. Under quasi-continuous reconnection at the high latitude site, the rotation of field lines and plasma generates a funnel along which upward FACs are established and electrons precipitate into the ionosphere, close to the magnetic pole. Such IMF conditions are met here: although quite low, the IMF B_Y and B_z components increase from the beginning of the 24 May as the solar wind density decreases. Notably, the polar spot appears prior to the arrival of the sub-Alfvénic solar wind (see Figure 1), suggesting that this system could have already been formed. The IMAGE/SI observations featuring the polar spot in Figure 4 also show a faint feature that could be an arm of the space hurricane, although its presence is not tracked.

The current system described in the space hurricane formation is also implied by the sub-Alfvénic observations here: a large convection cell is observed, centred on the pole, with evidence of electron acceleration in UV and radio aurora. While the Alfvén wings are established, the closed geomagnetic field lines become more symmetrical as the magnetotail flux joins the wings (Chané et al., 2015). Under northward IMF, open magnetic flux in the magnetosphere can close if the clock angle is close to zero (Fairfield et al., 1996; Y. Zhang et al., 2009; Milan et al., 2022). Under the two effects, the magnetosphere is thus expected to be dipolar at all MLTs. Such field lines on the dayside could host reconnection with the IMF at high magnetic latitudes to sustain the upward FAC of the space hurricane. The open field lines along the Alfvén wings also fall in the location of the upward FAC of the space hurricane; the formation of the Alfvén wing could aid the continued driving of the space hurricane, or vice versa. It could also be possible for further reconnection sites to be found along the Alfvén wing at low-shear angles.

When the sub-Alfvénic solar wind reaches Earth and the bowshock dissipates, the difference in inner magnetospheric and outer plasma environment changes drastically. As discussed, the typical magnetospheric configuration sees the magnetosphere separated from the IMF by the magnetopause, with the thermalised plasma of the magnetosheath lying between this and the solar wind; the plasma parameters (pressure, plasma beta) are significantly different between the two environments. Inside the magnetopause, the plasma beta β is lower as the magnetic pressure dominates. In the magnetosheath, the thermalised plasma behind the bowshock is typically dominated by kinetic pressure from the impact of the solar wind. As discussed by Chané et al. (2012), the low density, low β and sub-Alfvénic conditions of the solar wind result in the dissipation of the bowshock and a lack of shocked, thermalised plasma between the solar wind and the magnetopause. The typical pressure balance between kinetic ram pressure and magnetic pressure is thus replaced by more comparable conditions and β values between the solar wind and the magnetosphere. For this reason, the terrestrial magnetosphere in this case is similar to that of Mercury, where the magnetic pressure of the solar wind is more dominant and therefore the β of the magnetosphere is more comparable (Slavin & Holzer, 1981; Dibraccio et al., 2013). Recent work has shown that, due to the low difference in β values between the magnetosphere and magnetosheath of Mercury, component reconnection (reconnection outside of an antiparallel configuration) can occur at unusually low angles of magnetic shear (Sun et al., 2020; Zomerdijk-Russell et al., 2023). It is thus also possible that driving reconnection processes could take place along the field lines of the Alfvén wing itself. Given the orientation of the northern Alfvén wing, the field lines of the far Alfvén wing are oriented very closely with the IMF. In the sub-Alfvénic circumstances here, the low-shear reconnection may occur at a rate high enough to sustain the upward FAC of the space hurricane, and thus continue to produce the observed auroral emissions.

5 Summary

Between the 23-25 May 2002 the solar wind became sub-Alvénic due to an abnormally long period ($\sim$ 24 hours) of low plasma density. This lead to the formation of Alfvén wings at both magnetic poles of Earth, whose orientation and dynamics have been well-studied (Chané et al., 2012, 2015). The IMF conditions were, with a positive B_z component, such that the level of geomagnetic disturbance would be expected to be low, further influenced by the low kinetic pressure of the solar wind. By comparing the UV and radio auroral observations between periods of super-Alfvénic driving (Section 3.2), the period of sub-Alfvénic driving with established Alfvén wings (Section 3.3) and the period of transition between sub- and super-Alfvénic driving (Section 3.4) we have inferred a previously unobserved state of magnetosphere-ionosphere coupling during this interval. Using narrowband spectrographic observations of the UV aurora with IMAGE/SI, there is evidence of highly localised electron aurora at the northern magnetic pole whilst the Alfvén wings are present, with no other components present in the auroral zone. With remote radio observations of AKR we have observed the presence of electron acceleration that coincides with the polar aurora.

Multipoint, remote observations of AKR are useful for determining the morphology of the auroral acceleration region based on the anisotropic beaming of AKR sources (Olsson et al., 2004; Waters, Jackman, et al., 2021). During super-Alfvénic driving on 23 May, similar AKR morphology was observed with IMAGE/RPI and Wind/WAVES, the former being relatively close to Earth (within 7 R_E) while the latter was far away (300 R_E) in the afternoon LT sector. Such similarities, paired with the UV observations of the active auroral oval (see Figure 2), suggest that both observers were viewing common AKR sources distributed widely in longitude. During the sub-Alfvénic driving the radio observations show discrepancies that, with the localised polar spot, suggest AKR sources, and by proxy the region of electron acceleration, lie along a much more constrained flux tube.

The IMF conditions observed at Earth as the solar wind density decreases would, under more typical conditions, suggest the establishment of HiLDA or a space hurricane. Both phenomena occur following magnetic reconnection in the magnetosphere at high magnetic latitudes. For HiLDA and the particular case of space hurricanes (which could be seen as a special case of HiLDA given the similarities in its generation), electron acceleration is driven by an upward FAC that hosts a parallel electric field that sustains current continuity in the NBZ current system (Frey, 2007; Carter et al., 2018). During a space hurricane an upward FAC is established above the magnetic pole as continued lobe reconnection occurs under IMF conditions with a dominant B_Y component (Q. H. Zhang et al., 2021). The clockwise-rotating convection pattern that follows the plasma flow is centred on the pole. While we do not have continuous observations that allow direct inference of reconnection, infrequent observations by SuperDARN and DMSP suggest the presence of such a convection cell at the magnetic pole. This, paired with the evidence of constrained UV aurora and AKR intensification suggest the dominance of such a current system. These observations of AKR are the first of their kind, occurring with either HiLDA- or space hurricane-related UV aurora, and with levels of source amplification usually seen during super-Alfvénic driving and geomagnetically disturbed periods. The morphology of the Alfvén wings and the space hurricane dynamics, as well as the appearance of the polar spot prior to the arrival of the sub-Alfvénic solar wind, suggest that the formation or continuation of the space hurricane could interact with the Alfvén wing or vice-versa. The AKR observations also suggest an extension of the auroral acceleration region to lower altitudes along the host flux tube.

These observations show that driven electron acceleration can occur within the magnetosphere even when its global dynamics are expected to be suppressed, and demonstrate the extreme range of conditions that can invoke such coupling. The use of remote AKR observations is once more shown as a highly useful proxy for the development of the auroral acceleration region alongside other observations. The sub-Alfvénic driving of the magnetosphere also makes for an interesting comparison with the magnetosphere of Ganymede, which has a permanent Alfvén wing structure due to its location within the Jovian magnetosphere (Jia et al., 2010). While a comparative study of the systems during this period is out of the scope of this paper, it is interesting to note the vastly different auroral configurations; the terrestrial magnetosphere sees highly localised polar aurora while the magnetosphere of Ganymede shows a persistent auroral oval. This highlights the variety of dynamics that can be sustained under sub-Alfvénic driving and the potential for complex combinations of varied magnetospheric configurations and current systems.

6 Open Research

AKR-calibrated observations from Wind/WAVES can be found at `https://doi.org/10.25935/wxv0-vr90` (Waters, Cecconi, et al., 2021). Uncalibrated observations from Wind/WAVES can be found at CDAWeb (`https://cdaweb.gsfc.nasa.gov/`), using the "WI_H1_WAV" data set. Data from the RPI and SI instruments of the IMAGE spacecraft are available at CDAWeb (`https://cdaweb.gsfc.nasa.gov/`). Relevant RPI data are accessed by selecting the "IM_K1_RPI" data set. Relevant SI data are accessed by selecting the "IM_K0_SIE" and "IM_K0_SIP" data sets. ACE solar wind and IMF data are also available from CDAWeb, using the "AC_H0_SWE" and "AC_H0_MFI" data sets. PC indices are available at `https://pcindex.org/archive`. SuperDARN convection maps are available at `https://superdarn.ca/convection-maps`. DMSP/SSIES and DMSP/SSJ data are also available at CDAWeb (`https://cdaweb.gsfc.nasa.gov/`) and quicklook plots can be browsed at `https://dmsp.bc.edu/`.

Acknowledgments

J.E.W was supported by the Centre National d'Études Spatiales (CNES). The authors acknowledge CNES, CNRS (Centre National de la Recherche Scientifique), and Observatoire de Paris for support to the Wind/WAVES team and the CDPP (Centre de Donn´ees de la Physique des Plasmas) for the provision of the Wind/WAVES RAD1 L2 data. The authors acknowledge support from Paris Astronomical Data Centre (PADC) for the preparation and distribution of the data collection. S.E.M was supported by the Science and Technology Facilities Council (STFC), UK, grant no. ST/S000429/1. M.-T.W. acknowledges funding through the UKRI STFC Ernest Rutherford Fellowship Scheme (ST/X003663/1). The authors acknowledge the use of SuperDARN data. SuperDARN is a collection of radars funded by national scientific funding agencies of Australia, Canada, China, France, Italy, Japan, Norway, South Africa, United Kingdom and the United States of America.

References

Akasofu, S. I. (1964). The development of the auroral substorm. *Planetary and Space Science*, *12*(4), 273-282. doi: 10.1016/0032-0633(64)90151-5

Akasofu, S. I. (1981). Energy coupling between the solar wind and the magnetosphere. *Space Science Reviews*, *28*(2), 121-190. doi: 10.1007/BF00218810

Alexander, J. K., & Kaiser, M. L. (1976). Terrestrial kilometric radiation, 1. Spatial structure studies. *Journal of Geophysical Research*, *81*(34), 5948-5956. doi: 10.1029/JA081i034p05948

Alexander, J. K., & Kaiser, M. L. (1977). Terrestrial kilometric radiation, 2. Emission from the magnetospheric cusp and dayside magnetosheath. *Journal of Geophysical Research*, *82*(1), 98–104. doi: 10.1029/JA082i001p00098

Anderson, B. J., Korth, H., Waters, C. L., Green, D. L., Merkin, V. G., Barnes, R. J., & Dyrud, L. P. (2014). Development of large-scale Birkeland currents determined from the Active Magnetosphere and Planetary Electrodynamics Response Experiment. *Geophysical Research Letters*, *41*(9), 3017–3025. doi: 10.1002/2014GL059941

Anderson, B. J., Takahashi, K., & Toth, B. A. (2000). Sensing global Birkeland currents with iridium® engineering magnetometer data. *Geophysical Research Letters*, *27*(24), 4045-4048. doi: 10.1029/2000GL000094

Anderson, R. R., Matsumoto, H., Hashimoto, K., Kojima, H., Kasaba, Y., Kaiser, M. L., ... Rostoker, G. (2005). Geotail, Polar, and Wind Observations of Auroral Kilometric Radiation. *COSPAR Colloquia Series*, *16*(C), 205-219. doi: 10.1016/S0964-2749(05)80032-0

Baker, D. N., Hones, J., E. W., Payne, J. B., & Feldman, W. C. (1981). A high time resolution study of interplanetary parameter correlations with AE. *Geophysical Research Letters*, *8*(2), 179-182. doi: 10.1029/GL008i002p00179

Beedle, J. M., Chen, L. J., Shuster, J. R., Gurram, H., Gershman, D. J., Chen, Y., … Torbert, R. B. (2024). Field-Aligned Current Structures During the Terrestrial Magnetosphere's Transformation Into Alfvén Wings and Recovery. *Geophysical Research Letters*, *51*(13), e2024GL108839. doi: 10.1029/2024GL108839

Benson, R. F., Calvert, W., & Klumpar, D. M. (1980). Simultaneous wave and particle observations in the auroral kilometric radiation source region. *Geophysical Research Letters*, *7*(11), 959-962. doi: 10.1029/GL007i011p00959

Bougeret, J. L., Kaiser, M. L., Kellogg, P. J., Manning, R., Goetz, K., Monson, S. J., … Hoang, S. (1995). WAVES: The radio and plasma wave investigation on the wind spacecraft. *Space Science Reviews*, *71*(1-4), 231-263. doi: 10.1007/BF00751331

Brautigam, D. H., Gussenhoven, M. S., & Hardy, D. A. (1991). A statistical study on the effects of IMF B_z and solar wind speed on auroral ion and electron precipitation. *Journal of Geophysical Research*, *96*(A4), 5525-5538. doi: 10.1029/91JA00157

Browett, S. D., Fear, R. C., Grocott, A., & Milan, S. E. (2017). Timescales for the penetration of IMF By into the Earth's magnetotail. *Journal of Geophysical Research: Space Physics*, *122*(1), 579-593. doi: 10.1002/2016JA023198

Burkholder, B. L., Chen, L. J., Sarantos, M., Gershman, D. J., Argall, M. R., Chen, Y., … Gurram, H. (2024). Global Magnetic Reconnection During Sustained Sub-Alfvénic Solar Wind Driving. *Geophysical Research Letters*, *51*(6). doi: 10.1029/2024GL108311

Burton, R. K., McPherron, R. L., & Russell, C. T. (1975). An empirical relationship between interplanetary conditions and Dst. *Journal of Geophysical Research*, *80*(31), 4204. doi: 10.1029/JA080i031p04204

Carter, J. A., Milan, S. E., Fogg, A. R., Paxton, L. J., & Anderson, B. J. (2018). The Association of High-Latitude Dayside Aurora With NBZ Field-Aligned Currents. *Journal of Geophysical Research: Space Physics*, *123*(5), 3637-3645. doi: 10.1029/2017JA025082

Chané, E., Raeder, J., Saur, J., Neubauer, F. M., Maynard, K. M., & Poedts, S. (2015). Simulations of the Earth's magnetosphere embedded in sub-Alfvénic solar wind on 24 and 25 May 2002. *Journal of Geophysical Research: Space Physics*, *120*(10), 8517-8528. doi: 10.1002/2015JA021515

Chané, E., Saur, J., Neubauer, F. M., Raeder, J., & Poedts, S. (2012). Observational evidence of Alfvén wings at the Earth. *Journal of Geophysical Research: Space Physics*, *117*(9), A09217. doi: 10.1029/2012JA017628

Chané, E., Schmieder, B., Dasso, S., Verbeke, C., Grison, B., Démoulin, P., & Poedts, S. (2021). Over-expansion of a coronal mass ejection generates sub-Alfvénic plasma conditions in the solar wind at Earth. *Astronomy and Astrophysics*, *647*, A149. doi: 10.1051/0004-6361/202039867

Chen, L. J., Gershman, D., Burkholder, B., Chen, Y., Sarantos, M., Jian, L., … Burch, J. (2024). Earth's Alfvén Wings Driven by the April 2023 Coronal Mass Ejection. *Geophysical Research Letters*, *51*(14), e2024GL108894. doi: 10.1029/2024GL108894

Christensen, A. B., Lyons, L. R., Hecht, J. H., Sivjee, G. G., Meier, R. R., & Strickland, D. G. (1987). Magnetic field-aligned electric field acceleration and the characteristics of the optical aurora. *Journal of Geophysical Research*, *92*(A6), 6163-6167. doi: 10.1029/JA092iA06p06163

Chust, T., Roux, A., Kurth, W. S., Gurnett, D. A., Kivelson, M. G., & Khurana, K. K. (2005). Are Io's Alfvén wings filamented? Galileo observations. *Planetary and Space Science*, *53*(4), 395-412. doi: 10.1016/j.pss.2004.09.021

Coleman, I. J., Chisham, G., Pinnock, M., & Freeman, M. P. (2001). An ionospheric convection signature of antiparallel reconnection. *Journal of Geophysical Research*, *106*(A12), 28995-29008. doi: 10.1029/2001JA900084

Cowley, S. W. H. (1981). Magnetospheric asymmetries associated with the y-component of the IMF. *Planetary and Space Science*, *29*(1), 79-96. doi: 10.1016/0032-0633(81)90141-0

Crooker, N. U. (1979). Dayside merging and cusp geometry. *Journal of Geophysical Research*, *84*(A3), 951-959. doi: 10.1029/JA084iA03p00951

Crooker, N. U. (1992). Reverse convection. *Journal of Geophysical Research*, *97*(A12), 19363-19372. doi: 10.1029/92JA01532

Despirak, I. V., Kozelova, T. V., Kozelov, B. V., & Lubchich, A. A. (2020). Westward propagation of substorm by THEMIS and ground-based observations. *Journal of Atmospheric and Solar-Terrestrial Physics*, *206*, 105325. doi: 10.1016/j.jastp.2020.105325

Dibraccio, G. A., Slavin, J. A., Boardsen, S. A., Anderson, B. J., Korth, H., Zurbuchen, T. H., … Solomon, S. C. (2013). MESSENGER observations of magnetopause structure and dynamics at Mercury. *Journal of Geophysical Research: Space Physics*, *118*(3), 997-1008. doi: 10.1002/jgra.50123

Dungey, J. W. (1961). Interplanetary Magnetic Field and the Auroral Zones. *Phys. Rev. Lett.*, *6*(2), 47–48. Retrieved from `https://link.aps.org/doi/10.1103/PhysRevLett.6.47` doi: 10.1103/PhysRevLett.6.47

Dungey, J. W. (1965). The Length of the Magnetospheric Tail. *Journal of Geophysical Research*, *70*(7), 3918.

Elphic, R. C., Bonnell, J. W., Strangeway, R. J., Kepko, L., Ergun, R. E., McFadden, J. P., … Pfaff, R. (1998). The auroral current circuit and field-aligned currents observed by FAST. *Geophysical Research Letters*, *25*(12), 2033-2036. doi: 10.1029/98GL01158

Ergun, R. E., Carlson, C. W., McFadden, J. P., Delory, G. T., Strangeway, R. J., & Pritchett, P. L. (2000). Electron-Cyclotron Maser Driven by Charged-Particle Acceleration from Magnetic Field–aligned Electric Fields. *The Astrophysical Journal*, *538*(1), 456-466. doi: 10.1086/309094

Fairfield, D. H., Lepping, R. P., Frank, L. A., Ackerson, K. L., Paterson, W. R., Kokubun, S., … Nakamura, M. (1996). Geotail Observations of an Unusual Magnetotail under Very Northward IMF Conditions. *Journal of Geomagnetism and Geoelectricity*, *48*(5), 473-487. doi: 10.5636/jgg.48.473

Fear, R. C., Milan, S. E., Carter, J. A., & Maggiolo, R. (2015). The interaction between transpolar arcs and cusp spots. *Geophysical Research Letters*, *42*(22), 9685-9693. doi: 10.1002/2015GL066194

Feldstein, Y. I., & Starkov, G. V. (1970). The auroral oval and the boundary of closed field lines of geomagnetic field. *Planetary and Space Science*, *18*(4), 501-508. doi: 10.1016/0032-0633(70)90127-3

Fogg, A. R., Jackman, C. M., Waters, J. E., Bonnin, X., Lamy, L., Cecconi, B., … Louis, C. K. (2022). Wind/WAVES Observations of Auroral Kilometric Radiation: Automated Burst Detection and Terrestrial Solar Wind - Magnetosphere Coupling Effects. *Journal of Geophysical Research: Space Physics*, *127*(5), 1–21. doi: 10.1029/2021JA030209

Forsyth, C., Rae, I. J., Coxon, J. C., Freeman, M. P., Jackman, C. M., Gjerloev, J., & Fazakerley, A. N. (2015). A new technique for determining Substorm Onsets and Phases from Indices of the Electrojet (SOPHIE). *Journal of Geophysical Research: Space Physics*, *120*(12), 10592-10606. doi: 10.1002/2015JA021343

Frey, H. U. (2007). Localized aurora beyond the auroral oval. *Reviews of Geophysics*, *45*(1). doi: 10.1029/2005RG000174

Frey, H. U., Han, D., Kataoka, R., Lessard, M. R., Milan, S. E., Nishimura, Y., … Zou, Y. (2019). Dayside Aurora. *Space Science Reviews*, *215*(8). doi: 10.1007/s11214-019-0617-7

Frey, H. U., Immel, T. J., Lu, G., Bonnell, J., Fuselier, S. A., Mende, S. B., … Le,

G. (2003). Properties of localized, high latitude, dayside aurora. *Journal of Geophysical Research: Space Physics*, *108*(A4). doi: 10.1029/2002JA009332

Frey, H. U., Mende, S. B., Angelopoulos, V., & Donovan, E. F. (2004). Substorm onset observations by IMAGE-FUV. *Journal of Geophysical Research: Space Physics*, *109*(A10), A10304. doi: 10.1029/2004JA010607

Frey, H. U., Østgaard, N., Immel, T. J., Korth, H., & Mende, S. B. (2004). Seasonal dependence of localized, high-latitude dayside aurora (HiLDA). *Journal of Geophysical Research: Space Physics*, *109*(A4), A04303. doi: 10.1029/2003JA010293

Gjerloev, J. W. (2012). The SuperMAG data processing technique. *Journal of Geophysical Research: Space Physics*, *117*(9), 1-19. doi: 10.1029/2012JA017683

Gonzalez, W. D., Joselyn, J. A., Kamide, Y., Kroehl, H. W., Rostoker, G., Tsurutani, B. T., & Vasyliunas, V. M. (1994). What is a geomagnetic storm? *Journal of Geophysical Research*, *99*(A4), 5771-5792. doi: 10.1029/93JA02867

Gosling, J. T., Bame, S. J., McComas, D. J., & Phillips, J. L. (1990). Coronal mass ejections and large geomagnetic storms. *Geophysical Research Letters*, *17*(7), 901-904. doi: 10.1029/GL017i007p00901

Gosling, J. T., Thomsen, M. F., Bame, S. J., Elphic, R. C., & Russell, C. T. (1991). Observations of reconnection of interplanetary and lobe magnetic field lines at the high-latitude magnetopause. *Journal of Geophysical Research*, *96*(A8), 14097-14106. doi: 10.1029/91JA01139

Green, J. L., Saflekos, N. A., Gurnett, D. A., & Potemra, T. A. (1982). A correlation between auroral kilometric radiation and field-aligned currents. *Journal of Geophysical Research*, *87*(A12), 10463-10467. doi: 10.1029/JA087iA12p10463

Grocott, A., & Milan, S. E. (2014). The influence of IMF clock angle timescales on the morphology of ionospheric convection. *Journal of Geophysical Research: Space Physics*, *119*(7), 5861-5876. doi: 10.1002/2014JA020136

Gurnett, D. A. (1974). The Earth as a radio source: Terrestrial kilometric radiation. *Journal of Geophysical Research*, *79*(28), 4227–4238. doi: 10.1029/JA079i028p04227

Hajra, R., & Tsurutani, B. T. (2022). Near-Earth Sub-Alfvénic Solar Winds: Interplanetary Origins and Geomagnetic Impacts. *The Astrophysical Journal*, *926*(2), 135. doi: 10.3847/1538-4357/ac4471

Hanasz, J., Panchenko, M., De Feraudy, H., Schreiber, R., & Mogilevsky, M. M. (2003). Occurrence distributions of the auroral kilometric radiation ordinary and extraordinary wave modes. *Journal of Geophysical Research: Space Physics*, *108*(A11), 1408. doi: 10.1029/2002JA009579

Hashimoto, K., Matsumoto, H., Murata, T., Kaiser, M. L., & Bougeret, J.-L. (1998). Comparison of AKR simultaneously observed by the GEOTAIL and WIND spacecraft. *Geophysical Research Letters*, *25*(6), 853-856. doi: 10.1029/98GL00385

Hones, J., E. W. (1979). Transient Phenomena in the Magnetotail and Their Relation to Substorms. *Space Science Reviews*, *23*(3), 393-410. doi: 10.1007/BF00172247

Hones, J., E. W., Craven, J. D., Frank, L. A., Evans, D. S., & Newell, P. T. (1989). The horse-collar aurora: A frequent pattern of the aurora in quiet times. *Geophysical Research Letters*, *16*(1), 37-40. doi: 10.1029/GL016i001p00037

Huff, R. L., Calvert, W., Craven, J. D., Frank, L. A., & Gurnett, D. A. (1988). Mapping of auroral kilometric radiation sources to the aurora. *Journal of Geophysical Research*, *93*(A10), 11445. doi: 10.1029/JA093iA10p11445

Iijima, T., & Potemra, T. A. (1976). Field-aligned currents in the dayside cusp observed by triad. *Journal of Geophysical Research*, *81*(A34), 5971-5979. doi: 10.1029/JA081i034p05971

Iijima, T., & Potemra, T. A. (1978). Large-scale characteristics of field-aligned currents associated with substorms. *Journal of Geophysical Research*, *83*(A2), 599-615. doi: 10.1029/JA083iA02p00599

Jia, X., Walker, R. J., Kivelson, M. G., Khurana, K. K., & Linker, J. A. (2010). Dynamics of Ganymede's magnetopause: Intermittent reconnection under steady external conditions. *Journal of Geophysical Research: Space Physics*, *115*(12), A12202. doi: 10.1029/2010JA015771

Juusola, L., Østgaard, N., Tanskanen, E., Partamies, N., & Snekvik, K. (2011). Earthward plasma sheet flows during substorm phases. *Journal of Geophysical Research: Space Physics*, *116*(A10), A10228. doi: 10.1029/2011JA016852

Kamide, Y., Perreault, P. D., Akasofu, S. I., & Winningham, J. D. (1977). Dependence of substorm occurrence probability on the interplanetary magnetic field and on the size of the auroral oval. *Journal of Geophysical Research*, *82*(35), 5521. doi: 10.1029/JA082i035p05521

Kamide, Y., Richmond, A. D., & Matsushita, S. (1981). Estimation of ionospheric electric fields, ionospheric currents, and field-aligned currents from ground magnetic records. *Jounral of Geophysical Research*, *86*(A2), 801-813. doi: 10.1029/JA086iA02p00801

Kepko, L., Spanswick, E., Angelopoulos, V., Donovan, E., McFadden, J., Glassmeier, K. H., ... Singer, H. J. (2009). Equatorward moving auroral signatures of a flow burst observed prior to auroral onset. *Geophysical Research Letters*, *36*(24), L24104. doi: 10.1029/2009GL041476

Kilpua, E. K., Balogh, A., von Steiger, R., & Liu, Y. D. (2017). Geoeffective Properties of Solar Transients and Stream Interaction Regions. *Space Science Reviews*, *212*(3-4), 1271-1314. doi: 10.1007/s11214-017-0411-3

Kullen, A., & Karlsson, T. (2004). On the relation between solar wind, pseudobreakups, and substorms. *Journal of Geophysical Research: Space Physics*, *109*(A12), 1-20. doi: 10.1029/2004JA010488

Lin, C. S., & Hoffman, R. A. (1982). Observation of inverted-V electron precipitation. *Space Science Reviews*, *33*(4), 415-457. doi: 10.1007/BF00212420

Lu, S., Xing, Z.-Y., Zhang, Q.-H., Zhang, Y.-L., Ma, Y.-Z., Wang, X.-Y., ... Song, D. (2022). A statistical study of space hurricanes in the Northern Hemisphere. *Frontiers in Astronomy and Space Sciences*, *9*, 373. doi: 10.3389/fspas.2022.1047982

Marques de Souza Franco, A., Hajra, R., Echer, E., & José Alves Bolzan, M. (2021). Seasonal features of geomagnetic activity: A study on the solar activity dependence. *Annales Geophysicae*, *39*(5), 929-943. doi: 10.5194/angeo-39-929-2021

McComas, D. J., Bame, S. J., Barker, P., Feldman, W. C., Phillips, J. L., Riley, P., & Griffee, J. W. (1998). Solar Wind Electron Proton Alpha Monitor (SWEPAM) for the Advanced Composition Explorer. *Space Science Reviews*, *86*, 563-612. doi: 10.1023/A:1005040232597

McPherron, R. L., Russell, C. T., & Aubry, M. P. (1973). Satellite studies of magnetospheric substorms on August 15, 1968: 9. Phenomenological model for substorms. *Journal of Geophysical Research*, *78*(16), 3131. doi: 10.1029/JA078i016p03131

Mende, S. B., Heetderks, H., Frey, H. U., Lampton, M., Geller, S. P., Abiad, R., ... Trondsen, T. (2000). Far ultraviolet imaging from the IMAGE spacecraft. 2. Wideband FUV imaging. *Space Science Reviews*, *91*, 271-285. doi: 10.1023/A:1005227915363

Mende, S. B., Heetderks, H., Frey, H. U., Lampton, M., Geller, S. P., Habraken, S., ... Cogger, L. (2000). Far ultraviolet imaging from the IMAGE spacecraft. 1. System design. *Space Science Reviews*, *91*, 243-270. doi: 10.1023/A:1005271728567

Mende, S. B., Heetderks, H., Frey, H. U., Stock, J. M., Lampton, M., Geller, S. P., ... Lauche, H. (2000). Far ultraviolet imaging from the IMAGE spacecraft. 3. Spectral imaging of Lyman-α and OI 135.6 nm. *Space Science Reviews*, *91*, 287-318. doi: 10.1023/A:1005292301251

Menietti, J. D., & Burch, J. L. (1987). DE 1 observations of theta aurora plasma source regions and Birkeland current charge carriers. *Journal of Geophysical Research*, *92*(A7), 7503-7518. doi: 10.1029/JA092iA07p07503

Menietti, J. D., Mutel, R. L., Christopher, I. W., Hutchinson, K. A., & Sigwarth, J. B. (2011). Simultaneous radio and optical observations of auroral structures: Implications for AKR beaming. *Journal of Geophysical Research: Space Physics*, *116*(12), 1-9. doi: 10.1029/2011JA017168

Milan, S. E., Bower, G. E., Carter, J. A., Paxton, L. J., Anderson, B. J., & Hairston, M. R. (2022). Lobe Reconnection and Cusp-Aligned Auroral Arcs. *Journal of Geophysical Research: Space Physics*, *127*(6). doi: 10.1029/2021JA030089

Milan, S. E., Carter, J. A., Bower, G. E., Imber, S. M., Paxton, L. J., Anderson, B. J., ... Hubert, B. (2020). Dual-Lobe Reconnection and Horse-Collar Auroras. *Journal of Geophysical Research: Space Physics*, *125*(10), e28567. doi: 10.1029/2020JA028567

Milan, S. E., Clausen, L. B. N., Coxon, J. C., Carter, J. A., Walach, M.-T., Laundal, K., ... Anderson, B. J. (2017). Overview of Solar Wind–Magnetosphere–Ionosphere–Atmosphere Coupling and the Generation of Magnetospheric Currents. *Space Science Reviews*, *206*(1-4), 547-573. doi: 10.1007/s11214-017-0333-0

Milan, S. E., Grocott, A., Forsyth, C., Imber, S. M., Boakes, P. D., & Hubert, B. (2009). A superposed epoch analysis of auroral evolution during substorm growth, onset and recovery: open magnetic flux control of substorm intensity. *Annales Geophysicae*, *27*(2), 659–668. doi: 10.5194/angeo-27-659-2009

Milan, S. E., Lester, M., Cowley, S. W. H., & Brittnacher, M. (2000). Dayside convection and auroral morphology during an interval of northward interplanetary magnetic field. *Annales Geophysicae*, *18*(4), 436-444. Retrieved from `https://angeo.copernicus.org/articles/18/436/2000/` doi: 10.1007/s00585-000-0436-9

Milan, S. E., Provan, G., & Hubert, B. (2007). Magnetic flux transport in the Dungey cycle: A survey of dayside and nightside reconnection rates. *Journal of Geophysical Research: Space Physics*, *112*(A1), A01209. doi: 10.1029/2006JA011642

Morioka, A., Miyoshi, Y., Kurita, S., Kasaba, Y., Angelopoulos, V., Misawa, H., ... McFadden, J. P. (2013). Universal time control of AKR: Earth is a spin-modulated variable radio source. *Journal of Geophysical Research: Space Physics*, *118*(3), 1123–1131. doi: 10.1002/jgra.50180

Morioka, A., Miyoshi, Y., Tsuchiya, F., Misawa, H., Sakanoi, T., Yumoto, K., ... Donovan, E. F. (2007). Dual structure of auroral acceleration regions at substorm onsets as derived from auroral kilometric radiation spectra. *Journal of Geophysical Research: Space Physics*, *112*(A6), A06245. doi: 10.1029/2006JA012186

Mutel, R. L., Christopher, I. W., & Pickett, J. S. (2008). Cluster multispacecraft determination of AKR angular beaming. *Geophysical Research Letters*, *35*(7), L07104. doi: 10.1029/2008GL033377

Mutel, R. L., Gurnett, D. A., & Christopher, I. W. (2004). Spatial and temporal properties of AKR burst emission derived from Cluster WBD VLBI studies. *Annales Geophysicae*, *22*(7), 2625-2632. doi: 10.5194/angeo-22-2625-2004

Nakai, H., & Kamide, Y. (1983). Response of nightside auroral-oval boundaries to the interplanetary magnetic field. *Journal of Geophysical Research*, *88*(A5), 4005-4014. doi: 10.1029/JA088iA05p04005

Neubauer, F. (1980). Nonlinear standing Alfvén wave current system at Io: Theory. *Journal of Geophysical Research: Space Physics*, *85*(A3), 1171-1178. doi: 10.1029/ja085ia03p01171

Neubauer, F. M. (1998). The sub-Alfvénic interaction of the Galilean satellites with

the Jovian magnetosphere. *Journal of Geophysical Research*, *103*(E9), 19843-19866. doi: 10.1029/97JE03370
Newell, P. T., & Gjerloev, J. W. (2011). Evaluation of SuperMAG auroral electrojet indices as indicators of substorms and auroral power. *Journal of Geophysical Research: Space Physics*, *116*(A12), A12211. doi: 10.1029/2011JA016779
Olsson, A., Janhunen, P., Hanasz, J., Mogilevsky, M., Perraut, S., & Menietti, J. D. (2004). Observational study of generation conditions of substorm-associated low-frequency AKR emissions. *Annales Geophysicae*, *22*(10), 3571-3582. doi: 10.5194/angeo-22-3571-2004
Østgaard, N., Mende, S. B., Frey, H. U., & Sigwarth, J. B. (2005). Simultaneous imaging of the reconnection spot in the opposite hemispheres during northward IMF. *Geophysical Research Letters*, *32*(21), L21104. doi: 10.1029/2005GL024491
Pedersen, B. M., Pottelette, R., Eliasson, L., Murphree, J. S., Elphinstone, R. D., Bahnsen, A., & Jespersen, M. (1992). Auroral kilometric radiation from transpolar arcs. *Journal of Geophysical Research*, *97*(A7), 10567-10573. doi: 10.1029/92JA00410
Reiff, P. H., & Burch, J. L. (1985). IMF B_y-dependent plasma flow and Birkeland currents in the dayside magnetosphere: 2. A global model for northward and southward IMF. *Journal of Geophysical Research*, *90*(A2), 1595-1610. doi: 10.1029/JA090iA02p01595
Reinisch, B. W., Haines, D. M., Bibl, K., Cheney, G., Galkin, I. A., Huang, X., ... Reiff, P. (2000). The Radio Plasma Imager investigation on the IMAGE spacecraft. *Space Science Reviews*, *91*, 319-359. doi: 10.1023/A:1005252602159
Ridley, A. J. (2007). Alfvén wings at Earth's magnetosphere under strong interplanetary magnetic fields. *Annales Geophysicae*, *25*(2), 533-542. doi: 10.5194/angeo-25-533-2007
Ridley, A. J., Lu, G., Clauer, C. R., & Papitashvili, V. O. (1998). A statistical study of the ionospheric convection response to changing interplanetary magnetic field conditions using the assimilative mapping of ionospheric electrodynamics technique. *Journal of Geophysical Research*, *103*(A3), 4023-4040. doi: 10.1029/97JA03328
Rothwell, P. L., Silevitch, M. B., & Block, L. P. (1984). A model for the propagation of the westward traveling surge. *Journal of Geophysical Research*, *89*(A10), 8941-8948. doi: 10.1029/JA089iA10p08941
Sandholt, P. E., Farrugia, C. J., Øieroset, M., Stauning, P., & Cowley, S. W. H. (1996). Auroral signature of lobe reconnection. *Geophysical Research Letters*, *23*(14), 1725-1728. doi: 10.1029/96GL01846
Slavin, J. A., & Holzer, R. E. (1981). Solar wind flow about the terrestrial planets 1. Modeling bow shock position and shape. *Journal of Geophysical Research: Space Physics*, *86*(A13), 11401-11418. doi: 10.1029/ja086ia13p11401
Smith, C. W., L'Heureux, J., Ness, N. F., Acuña, M. H., Burlaga, L. F., & Scheifele, J. (1998). The ACE Magnetic Fields Experiment. *Space Science Reviews*, *86*, 613-632. doi: 10.1023/A:1005092216668
Song, P., DeZeeuw, D. L., Gombosi, T. I., Groth, C. P. T., & Powell, K. G. (1999). A numerical study of solar wind-magnetosphere interaction for northward interplanetary magnetic field. *Journal of Geophysical Research*, *104*(A12), 28361-28378. doi: 10.1029/1999JA900378
Sonnerup, B. U. Ö. (1974). Magnetopause reconnection rate. *Journal of Geophysical Research*, *79*(10), 1546-1549. doi: 10.1029/JA079i010p01546
Stauning, P. (2013). The Polar Cap index: A critical review of methods and a new approach. *Journal of Geophysical Research: Space Physics*, *118*(8), 5021-5038. doi: 10.1002/jgra.50462
Strickland, D. J., Jasperse, J. R., & Whallen, J. A. (1983). Dependence of auroral FUV emissions on the incident electron spectrum and neutral at-

mosphere. *Journal of Geophysical Research*, *88*(A10), 8051-8062. doi: 10.1029/JA088iA10p08051

Sun, W. J., Slavin, J. A., Smith, A. W., Dewey, R. M., Poh, G. K., Jia, X., … Zhao, J. T. (2020). Flux Transfer Event Showers at Mercury: Dependence on Plasma β and Magnetic Shear and Their Contribution to the Dungey Cycle. *Geophysical Research Letters*, *47*(21). doi: 10.1029/2020GL089784

Treumann, R. A. (2006). The electron-cyclotron maser for astrophysical application. *Astronomy and Astrophysics Review*, *13*(4), 229–315. doi: 10.1007/s00159-006-0001-y

Troshichev, O. A., & Andrezen, V. G. (1985). The relationship between interplanetary quantities and magnetic activity in the southern polar cap. *Planetary and Space Science*, *33*(4), 415-419. doi: 10.1016/0032-0633(85)90086-8

Usmanov, A. V., Goldstein, M. L., Ogilvie, K. W., Farrell, W. M., & Lawrence, G. R. (2005). Low-density anomalies and sub-Alfvénic solar wind. *Journal of Geophysical Research: Space Physics*, *110*(A1), A01106. doi: 10.1029/2004JA010699

Vennerstroem, S. (2001). Interplanetary sources of magnetic storms: A statistical study. *Journal of Geophysical Research*, *106*(A12), 29175-29184. doi: 10.1029/2001JA000004

Walach, M. T., Grocott, A., Thomas, E. G., & Staples, F. (2022). Dusk-Dawn Asymmetries in SuperDARN Convection Maps. *Journal of Geophysical Research: Space Physics*, *127*(12), e2022JA030906. doi: 10.1029/2022JA030906

Waters, J. E., Cecconi, B., Jackman, C. M., Whiter, D. K., Bonnin, X., & Lamy, L. (2021). Wind/WAVES flux density collection calibrated for Auroral Kilometric Radiation (Version 1.0) [Dataset]. *PADC*. doi: 10.25935/wxv0-vr90

Waters, J. E., Jackman, C. M., Lamy, L., Cecconi, B., Whiter, D. K., Bonnin, X., … Fogg, A. R. (2021). Empirical Selection of Auroral Kilometric Radiation During a Multipoint Remote Observation With Wind and Cassini. *Journal of Geophysical Research: Space Physics*, *126*(10), 1-26. doi: 10.1029/2021JA029425

Waters, J. E., Jackman, C. M., Whiter, D. K., Fogg, A. R., Lamy, L., Carter, J. A., … Gallagher, P. (2023). Auroral Emissions and Inner Magnetospheric Dynamics During Earth's Response to the 28th October 2021 Coronal Mass Ejection. In C. K. Louis, C. M. Jackman, G. Fischer, A. H. Sulaiman, & P. Zucca (Eds.), *Planetary, Solar and Heliospheric Radio Emissions IX* (p. 104047). doi: 10.25546/104047

Waters, J. E., Jackman, C. M., Whiter, D. K., Forsyth, C., Fogg, A. R., Lamy, L., … Issautier, K. (2022). A Perspective on Substorm Dynamics Using 10 Years of Auroral Kilometric Radiation Observations From Wind. *Journal of Geophysical Research: Space Physics*, *127*(9), e30449. doi: 10.1029/2022JA030449

Wilcox, J. M., Schatten, K. H., & Ness, N. F. (1967). Influence of interplanetary magnetic field and plasma on geomagnetic activity during quiet-sun conditions. *Journal of Geophysical Research*, *72*(1), 19-26. doi: 10.1029/JZ072i001p00019

Zhang, J., Liemohn, M. W., Kozyra, J. U., Lynch, B. J., & Zurbuchen, T. H. (2004). A statistical study of the geoeffectiveness of magnetic clouds during high solar activity years. *Journal of Geophysical Research: Space Physics*, *109*(A9), A09101. doi: 10.1029/2004JA010410

Zhang, Q. H., Zhang, Y. L., Wang, C., Oksavik, K., Lyons, L. R., Lockwood, M., … Xia, L. D. (2021). A space hurricane over the Earth's polar ionosphere. *Nature Communications*, *12*(1), 1207. doi: 10.1038/s41467-021-21459-y

Zhang, Y., Paxton, L. J., Newell, P. T., & Meng, C. I. (2009). Does the polar cap disappear under an extended strong northward IMF? *Journal of Atmospheric and Solar-Terrestrial Physics*, *71*(17-18), 2006-2012. doi: 10.1016/j.jastp.2009.09.005

Zhu, L., Schunk, R. W., & Sojka, J. J. (1997). Polar cap arcs: a review. *Journal of Atmospheric and Solar-Terrestrial Physics*, *59*, 1087-1126. doi: 10.1016/S1364-6826(96)00113-7

Zmuda, A. J., Martin, J. H., & Heuring, F. T. (1966). Transverse magnetic disturbances at 1100 kilometers in the auroral region. *Journal of Geophysical Research*, *71*(21), 5033-5045. doi: 10.1029/JZ071i021p05033

Zomerdijk-Russell, S., Masters, A., Sun, W. J., Fear, R. C., & Slavin, J. A. (2023). Does Reconnection Only Occur at Points of Maximum Shear on Mercury's Dayside Magnetopause? *Journal of Geophysical Research: Space Physics*, *128*(11), e2023JA031810. doi: 10.1029/2023JA031810